

# Structure and stability of steady porous medium convection at large Rayleigh number

Baole Wen<sup>1,2</sup>, Lindsey T. Corson<sup>3</sup> and Gregory P. Chini<sup>1,2,4,†</sup>

<sup>1</sup>Program in Integrated Applied Mathematics, University of New Hampshire, Durham, NH 03824, USA

<sup>2</sup>Center for Fluid Physics, University of New Hampshire, Durham, NH 03824, USA

<sup>3</sup>Department of Mathematics and Statistics, University of Strathclyde, 26 Richmond Street, Glasgow G1 1XH, UK

<sup>4</sup>Department of Mechanical Engineering, University of New Hampshire, Durham, NH 03824, USA

(Received 30 September 2014; revised 3 February 2015; accepted 30 March 2015;  
first published online 5 May 2015)

A systematic investigation of unstable steady-state solutions of the Darcy–Oberbeck–Boussinesq equations at large values of the Rayleigh number  $Ra$  is performed to gain insight into two-dimensional porous medium convection in domains of varying aspect ratio  $L$ . The steady convective states are shown to transport less heat than the statistically steady ‘turbulent’ flow realised at the same parameter values: the Nusselt number  $Nu \sim Ra$  for turbulent porous medium convection, while  $Nu \sim Ra^{0.6}$  for the maximum heat-transporting steady solutions. A key finding is that the lateral scale of the heat-flux-maximising solutions shrinks roughly as  $L \sim Ra^{-0.5}$ , reminiscent of the decrease of the mean inter-plume spacing observed in turbulent porous medium convection as the thermal forcing is increased. A spatial Floquet analysis is performed to investigate the linear stability of the fully nonlinear steady convective states, extending a recent study by Hewitt *et al.* (*J. Fluid Mech.*, vol. 737, 2013, pp. 205–231) by treating a base convective state, and secondary stability modes, that satisfy appropriate boundary conditions along plane parallel walls. As in that study, a bulk instability mode is found for sufficiently small-aspect-ratio base states. However, the growth rate of this bulk mode is shown to be significantly reduced by the presence of the walls. Beyond a certain critical  $Ra$ -dependent aspect ratio, the base state is most strongly unstable to a secondary mode that is localised near the heated and cooled walls. Direct numerical simulations, strategically initialised to investigate the fully nonlinear evolution of the most dangerous secondary instability modes, suggest that the (long time) mean inter-plume spacing in statistically steady porous medium convection results from a balance between the competing effects of these two types of instability.

**Key words:** convection in porous media, instability, pattern formation

## 1. Introduction

Porous medium convection is a key environmental process that has been extensively studied since the 1940s (Horton & Rogers 1945; Lapwood 1948) due to its numerous

† Email address for correspondence: [greg.chini@unh.edu](mailto:greg.chini@unh.edu)

geoscientific applications including oil recovery, groundwater flow and geothermal energy extraction (Phillips 1991, 2009; Nield & Bejan 2006). More fundamentally, as a paradigm for forced-dissipative infinite-dimensional nonlinear dynamical systems, buoyancy-driven convection in a fluid-saturated porous layer retains much of the rich dynamics of Rayleigh–Bénard convection in a pure fluid layer yet provides a simpler physical and mathematical setting for studying instabilities, bifurcations, pattern formation and spatiotemporally chaotic dynamics. Recently, this system has again become the subject of intense scrutiny due to applications in carbon dioxide sequestration in terrestrial aquifers, one promising means of reducing the emission of greenhouse gases into the atmosphere (Metz *et al.* 2005).

The flow in a horizontal porous layer uniformly heated from below undergoes a sequence of bifurcations as the Rayleigh number  $Ra$ , the normalised temperature drop across the layer, is increased. When  $Ra > 4\pi^2$ , the simple conduction solution becomes linearly unstable (Nield & Bejan 2006) and steady  $O(1)$  aspect-ratio large-scale convection rolls emerge. In a two-dimensional (2D) domain, the steady rolls strengthen but remain stable as  $Ra$  is increased up to  $Ra \approx 400$  (Schubert & Straus 1982). For  $Ra$  slightly greater than 400, instabilities within the upper and lower thermal boundary layers generate small-scale features that are advected around the cell by the large-scale rolls. In this moderate- $Ra$  parameter regime,  $400 \lesssim Ra \lesssim 1300$ , the resulting flow exhibits a series of transitions between periodic and quasi-periodic roll motions, as discussed in considerable detail by Kimura, Schubert & Straus (1986, 1987), Aidun & Steen (1987) and Graham & Steen (1992, 1994). However, the rolls do not completely lose coherence until  $Ra \gtrsim 1300$ . The overall dynamics is then better characterised as spatiotemporally chaotic plume shedding from the boundaries rather than quasi-coherent cellular flow (Otero *et al.* 2004; Hewitt, Neufeld & Lister 2012). This marks the transition to the ‘turbulent’ high- $Ra$  regime.

The direct numerical simulations (DNS) of Hewitt *et al.* (2012) reveal that at large  $Ra$  porous medium convection exhibits a three-region asymptotic structure: adjacent to the upper and lower walls are extremely thin thermal boundary layers, with a thickness that scales as  $O(Ra^{-1})$ ; the interior region is dominated by a nearly vertical columnar exchange flow (‘mega-plumes’) spanning the height of the domain; and the transition zone between these regions is characterised by a series of small ‘proto-plumes’ that grow from the boundaries and merge with the interior mega-plumes. Remarkably, as  $Ra$  is increased, the interior columnar exchange flow becomes increasingly well organised. Hewitt *et al.* (2012) model this interior flow analytically using a single horizontal Fourier-mode ‘heat-exchanger’ solution, and extract a  $Ra^{-0.4}$  scaling for the time-mean inter-plume spacing from their simulation data. In a subsequent investigation, Hewitt, Neufeld & Lister (2013) show that the vertical columnar exchange flow is unstable for horizontal wavenumbers  $k$  greater than  $k \sim Ra^{5/14}$  as  $Ra \rightarrow \infty$ , in evident agreement with their DNS results. However, their stability analysis employs the analytical heat-exchanger model – in which the upper and lower boundaries are ignored – as the pertinent base flow on the grounds that  $k$  is not controlled directly by the small-scale dynamics of proto-plumes near the boundary, since these have a lateral scale of  $Ra^{-1}$ . Nevertheless, the relevance of their stability analysis remains an open question, since the influence of the boundaries is ignored. Our view is that it is preferable to analyse the stability of (numerically) exact solutions of the complete dynamical system (i.e. in which the base flow exactly satisfies the governing equations and all boundary conditions) that also exhibit certain flow structures observed in the time-dependent simulations. Specifically, the objective of our investigation is to determine the structure and

secondary stability of steady cellular solutions in porous medium convection at large Rayleigh number. Although our study is restricted to 2D configurations, we note that recent DNS of Rayleigh–Bénard convection in a three-dimensional (3D) porous layer at large Rayleigh number clearly exhibit the emergence of a three-region asymptotic structure, with an interior flow that is increasingly well described by an extension of the heat-exchanger model that consists of mega-plumes whose spacing decreases approximately as  $Ra^{-0.5}$  (Hewitt, Neufeld & Lister 2014). Thus, we may reasonably expect the results of our 2D investigation to provide at least partial insight into 3D porous medium convection, too.

The structure and stability of steady 2D porous medium convection at small to moderate Rayleigh number has been discussed in detail in many previous studies (Elder 1967; Palm, Weber & Kvernfold 1972; Horne & O’Sullivan 1974; Schubert & Straus 1982; Aidun & Steen 1987; Kimura *et al.* 1987; Graham & Steen 1992, 1994). The study of high-Rayleigh-number steady solutions, however, has been rather limited, in part because these solutions are unstable and exhibit fine-scale spatial structure. In the present work, we overcome these difficulties by numerically solving the steady governing equations using a Newton–Kantorovich iteration scheme (Boyd 2000). By investigating the dependence of the steady solutions on the domain aspect ratio  $L$ , we find that there exist two qualitatively distinct types of steady convective states at large  $Ra$ : for small  $L$ , the flow has the heat-exchanger structure in the interior identified by Hewitt *et al.* (2012); however, as  $L$  is increased, the steady convection develops a stably stratified core with a horizontal structure involving multiple Fourier modes. Comparison of the steady solutions with the long-time-averaged columnar flow observed in the DNS reveals that the latter is neither a heat exchanger nor a stably stratified core solution but instead combines certain attributes of both types of steady solutions.

After characterising these steady convective states as a function of  $Ra$  and  $L$ , we assess their stability to small-amplitude disturbances using Floquet theory. The Floquet technique was first introduced as a tool for secondary stability analysis in fluid dynamics by Kelly (1967), who applied this method to inviscid shear flows. Since then, Floquet analysis has been applied to numerous other shear and convective flows, including thermal convection (Busse 1967, 1972; Clever & Busse 1974), viscous shear flows (Herbert 1983, 1988; Orszag & Patera 1983) and Langmuir circulation (Tandon & Leibovich 1995; Chini, Julien & Knobloch 2009). In this paper, we follow Chini *et al.* (2009) by employing a Fourier–Chebyshev spectral method to discretise the differential eigenvalue problem derived from linearising the governing equations of porous medium convection about the fully nonlinear steady states. Our analysis reveals the existence of two types of instability for different  $L$  at large  $Ra$ : a bulk instability in which the most unstable disturbance spans the convective layer, and a wall instability in which the most unstable disturbance is strongly localised near the hot and cold boundaries.

We explore the nonlinear evolution of these secondary instabilities using high-resolution DNS. Both the bulk and the wall instability modes are shown to influence the mean inter-plume spacing at large  $Ra$ . To obtain a reliable estimate of this mean spacing the aspect ratio of the computational domain must be sufficiently large to capture long-wavelength secondary instabilities. We quantify this inter-plume spacing by performing DNS at extreme values of  $Ra$ , up to  $O(10^5)$ , in large- $L$  domains containing more than 15 pairs of plumes. The simulations show that the interior columnar exchange flow becomes very well organised for  $Ra \geq 39\,716$ , and that, at a given large  $Ra$ , there exists a small range of preferred plume spacings for which the

bulk and wall instabilities are balanced so that the interior columnar exchange flow is statistically steady.

The remainder of this paper is organised as follows. In the next section, we formulate the standard mathematical model of porous medium convection and recall the key results of linear stability theory for this system. In §3, we outline the numerical method used to find (generally unstable) steady high- $Ra$  solutions, describe the structure of these solutions for different aspect ratios, document the variation of heat transport with aspect ratio, identify the steady flows that maximise the heat transport as a function of both  $Ra$  and  $L$ , and quantitatively compare the mean interior columnar exchange flow manifested in DNS with the interior structure of the steady solutions. Using Floquet theory, we analyse the stability of these steady convective states in §4. In §5, we perform DNS strategically initialised with a superposition of the steady solutions and a small-amplitude contribution of the most unstable secondary instability eigenfunction to investigate how these steady states evolve into the statistically steady but spatiotemporally chaotic (turbulent) convective flow. Moreover, new results for the mean inter-plume spacing in porous medium convection for  $Ra = O(10^5)$  are also presented. Our conclusions are given in §6.

## 2. Problem formulation

We consider a 2D fluid-saturated porous layer in a domain of aspect ratio  $L$  that is heated from below at  $z = 0$  and cooled from above at  $z = 1$ . For simplicity as well as for consistency with the numerous prior stability, dynamical systems and computational investigations of porous medium convection in a Rayleigh–Bénard configuration referenced in §1, the evolution of the 2D velocity  $\mathbf{u}(\mathbf{x}, t) = (u, w)$ , temperature  $T(\mathbf{x}, t)$  and pressure  $p(\mathbf{x}, t)$  fields is presumed to be governed by the non-dimensional Darcy–Oberbeck–Boussinesq equations (Nield & Bejan 2006) in the infinite Darcy–Prandtl number limit:

$$\partial_t T + \mathbf{u} \cdot \nabla T = \nabla^2 T, \quad (2.1)$$

$$\mathbf{u} + \nabla p = Ra T \mathbf{e}_z (\Rightarrow \nabla^2 w = Ra \partial_x^2 T), \quad (2.2)$$

$$\nabla \cdot \mathbf{u} = 0, \quad (2.3)$$

where  $x$  and  $z$  are the horizontal and vertical coordinates respectively,  $\mathbf{e}_z$  is a unit vector in the  $z$  direction and  $\nabla^2$  is the 2D Laplacian operator. Strictly, these equations are only valid when there is no exchange of heat between the fluid and the solid matrix or when the heat capacities per unit volume of the fluid and the solid are equal. However, (2.1)–(2.3) are formally identical to the appropriately non-dimensionalised equations governing solutal convection, which is, of course, the more relevant interpretation for convective and diffusive transport of carbon dioxide in the sequestration context and for which no flux of solute between the fluid and solid is an appropriate idealisation. Moreover, the assumption of local thermal equilibrium can be shown to be a reasonable approximation in many applications for which rapid thermal adjustment of the solid matrix may be expected, as is often the case for small-pore media such as fibrous insulation (Nield & Bejan 2006; Bejan 2013).

Equations (2.1)–(2.3) are solved subject to the boundary conditions

$$T(x, 0, t) = 1, \quad T(x, 1, t) = 0, \quad w(x, 0, t) = 0, \quad w(x, 1, t) = 0 \quad (2.4a–d)$$

and  $L$ -periodicity of all fields in  $x$ . The Rayleigh number  $Ra$  appearing in (2.2) is a dimensionless parameter quantifying the ratio of driving to damping forces:

$$Ra = \frac{\alpha g (T_{bot} - T_{top}) KH}{\nu \kappa}, \quad (2.5)$$



where  $\alpha$  is the thermal expansion coefficient,  $g$  is the gravitational acceleration,  $T_{bot} - T_{top}$  is the dimensional temperature difference across the layer,  $K$  is the Darcy permeability coefficient,  $H$  is the layer depth,  $\nu$  is the kinematic viscosity and  $\kappa$  is the thermal diffusivity. A second control parameter governing the behaviour of this system is the domain aspect ratio  $L$ . One of the key quantities of interest in convection is the Nusselt number  $Nu$ , the ratio of the heat transport in the presence of convective motion to the conductive heat transport when  $\mathbf{u} = \mathbf{0}$ :

$$Nu = 1 + \frac{1}{L} \left\langle \int wT \, dx \, dz \right\rangle, \tag{2.6}$$

where the angle brackets denote a long-time average; i.e. for some function  $f$

$$\langle f \rangle = \lim_{\bar{t} \rightarrow \infty} \frac{1}{\bar{t}} \int_0^{\bar{t}} f \, dt. \tag{2.7}$$

From the equations of motion an alternative but equivalent expression for the Nusselt number can be derived,

$$Nu = -\frac{1}{L} \left\langle \int_{z=0} \partial_z T \, dx \right\rangle \equiv -\langle \partial_z \bar{T} |_{z=0} \rangle = \frac{1}{L} \langle \|\nabla T\|^2 \rangle, \tag{2.8}$$

where  $\bar{f} = 1/L \int_0^L f \, dx$  and  $\|f\| = (\int |f|^2 \, dx \, dz)^{1/2}$ .

One elementary solution of this system is the conduction state:  $T = 1 - z$ ,  $\mathbf{u} = \mathbf{0}$  and  $p = Ra(z - z^2/2)$ . A linear stability analysis can be performed by setting  $T = (1 - z) + \theta^*(x, z, t)$  and  $\mathbf{u} = (u^*, w^*)$ , where  $\theta^*$ ,  $u^*$  and  $w^*$  are small perturbations, and linearising (2.1)–(2.3) about the conduction solution. As first shown by Horton & Rogers (1945) and Lapwood (1948), the resulting (normalised) eigenfunctions are

$$\theta^* = \cos(kx) \sin(m\pi z) e^{\lambda^* t}, \quad w^* = \frac{Ra k^2}{m^2 \pi^2 + k^2} \cos(kx) \sin(m\pi z) e^{\lambda^* t}, \tag{2.9a,b}$$

with the corresponding eigenvalue

$$\lambda^* = \frac{Ra k^2}{m^2 \pi^2 + k^2} - (m^2 \pi^2 + k^2) \tag{2.10}$$

representing the growth rate of the given eigenmode. The eigenvalues for different  $Ra$ , vertical mode number  $m \geq 1$  and (continuous) horizontal wavenumber  $k$  (in an infinitely wide domain) are strictly real, implying that the onset of convection is to steady cells, and the largest growth rates occur for  $m = 1$ . By setting  $\lambda^* = 0$  with  $m = 1$ , an expression for the marginal stability boundary of the conduction state can be obtained:  $Ra = (\pi^2 + k^2)^2/k^2$ . We denote the high-wavenumber branch of marginal modes by

$$k_c = \frac{\sqrt{Ra} + \sqrt{Ra - 4\pi^2}}{2}, \tag{2.11}$$

and we define  $L_c = 2\pi/k_c$  as the corresponding wavelength of these marginal modes. At a given  $Ra > 4\pi^2$ , the conduction solution will become linearly unstable for aspect ratios  $L > L_c$ . Alternatively, by setting  $\partial \lambda^* / \partial k = 0$ , we find that the wavenumber  $k_f$  of

the fastest-growing linear mode is given by

$$k_f = \sqrt{\sqrt{Ra}\pi - \pi^2}. \tag{2.12}$$

We define  $L_f = 2\pi/k_f$  as the corresponding wavelength of this fastest-growing linear mode. In the limit  $Ra \rightarrow \infty$ ,  $k_f \sim \sqrt{\pi Ra}^{1/4}$  while  $k_c \sim Ra^{1/2}$ .

### 3. Steady convective states

#### 3.1. Newton–Kantorovich method

Following Corson (2011), we solve the steady version of the governing equations (2.1)–(2.3) numerically using a Newton–Kantorovich (NK) iterative scheme (Boyd 2000). It is convenient to first introduce a stream function  $\psi$  to describe the fluid velocity, so that  $(u, w) = (\partial_z\psi, -\partial_x\psi)$ . Then the time-independent dimensionless equations can be written as

$$\nabla^2\psi = -Ra \partial_x\theta, \tag{3.1}$$

$$\partial_z\psi \partial_x\theta - \partial_x\psi \partial_z\theta = -\partial_x\psi + \nabla^2\theta, \tag{3.2}$$

where  $\theta(x, z) = T(x, z) - (1 - z)$ , and  $\theta$  and  $\psi$  satisfy  $L_s$ -periodic boundary conditions in  $x$  and homogeneous Dirichlet boundary conditions in  $z$ . To avoid ambiguity,  $L_s$  is used here and throughout to denote the domain width associated with a given steady state. The solution of (3.1) and (3.2) can be expressed as

$$\begin{bmatrix} \theta \\ \psi \end{bmatrix} = \sum_{n=-N/2}^{N/2} \begin{bmatrix} \hat{\theta}_n(z) \\ \hat{\psi}_n(z) \end{bmatrix} e^{ink_sx} = \sum_{n=-N/2}^{N/2} \sum_{m=0}^M \begin{bmatrix} a_{mn} \\ b_{mn} \end{bmatrix} T_m(z) e^{ink_sx}, \tag{3.3}$$

where  $k_s = 2\pi/L_s$  is the fundamental wavenumber of the spatially periodic steady solution,  $M$  is the vertical truncation mode number,  $N$  is the horizontal truncation mode number and  $T_m(z)$  is the  $m$ th Chebyshev polynomial. In each  $L_s \times 1$  computational domain we seek steady solutions with reflection symmetry about  $x = L_s/2$  and centrosymmetry within each of the two  $L_s/2 \times 1$  subdomains which contain a single convection cell. These symmetry constraints require

$$a_{mn} \text{ is real; } b_{mn} \text{ is imaginary; } a_{mn} = b_{mn} = 0 \text{ if } (m + n) \text{ is even.} \tag{3.4}$$

To employ the NK algorithm, we rearrange (3.1) and (3.2) into the following form:

$$\nabla^2\psi = F^\psi(\theta_x), \tag{3.5}$$

$$\nabla^2\theta = F^\theta(\psi_x, \psi_z, \theta_x, \theta_z), \tag{3.6}$$

where a subscript denotes a partial derivative with respect to the given variable. Suppose the  $i$ th iterates  $\theta^i(x, z)$  and  $\psi^i(x, z)$  in the NK scheme are good approximations to the true solution  $\theta(x, z)$  and  $\psi(x, z)$ . Taylor expansion of the functionals  $F^\psi$  and  $F^\theta$  in (3.5) and (3.6) about these iterates yields

$$\nabla^2\psi = (F^\psi)^i + (F^\psi_{\theta_x})^i[\theta_x - \theta_x^i] + O([\theta_x - \theta_x^i]^2), \tag{3.7}$$

$$\begin{aligned} \nabla^2\theta &= (F^\theta)^i + (F^\theta_{\psi_x})^i[\psi_x - \psi_x^i] + (F^\theta_{\psi_z})^i[\psi_z - \psi_z^i] + (F^\theta_{\theta_x})^i[\theta_x - \theta_x^i] \\ &\quad + (F^\theta_{\theta_z})^i[\theta_z - \theta_z^i] + O([\psi_x - \psi_x^i]^2, [\psi_z - \psi_z^i]^2, [\theta_x - \theta_x^i]^2, [\theta_z - \theta_z^i]^2), \end{aligned} \tag{3.8}$$

where, for example,  $F_{\psi_x}^\theta$  denotes the Frechet derivative of the function  $F^\theta(\psi_x, \psi_z, \theta_x, \theta_z)$  with respect to  $\psi_x$ . After defining the correction terms

$$\Delta^\psi = \psi^{i+1} - \psi^i, \quad \Delta^\theta = \theta^{i+1} - \theta^i \tag{3.9a,b}$$

and evaluating the Frechet derivatives, the linear differential equations for the corrections can be expressed as

$$\nabla^2 \Delta^\psi + Ra D_x \Delta^\theta = -Ra \theta_x^i - \nabla^2 \psi^i, \tag{3.10}$$

$$[-D_x + \theta_z^i D_x - \theta_x^i D_z] \Delta^\psi + [\nabla^2 - \psi_z^i D_x + \psi_x^i D_z] \Delta^\theta = \psi_z^i \theta_x^i - \psi_x^i \theta_z^i + \psi_x^i - \nabla^2 \theta^i, \tag{3.11}$$

where  $D_x$  and  $D_z$  denote the first partial derivative operators with respect to  $x$  and  $z$ . According to the symmetry constraints (3.4), the solution (3.3) has the following form:

$$\theta = \hat{\theta}_0(z) + 2 \sum_{n=1}^{N/2} \hat{\theta}_n(z) \cos(nk_s x), \quad \psi = 2 \sum_{n=1}^{N/2} -\hat{\phi}_n(z) \sin(nk_s x), \tag{3.12a,b}$$

where  $\hat{\phi}_n \equiv \text{Im}\{\hat{\psi}_n\}$  is real. Then, for a given horizontal wavenumber  $nk_s$ , (3.10) and (3.11) become

$$-[D_{zz} - (nk_s)^2] \Delta^{\hat{\phi}_n} - nk_s Ra \Delta^{\hat{\theta}_n} = nk_s Ra \hat{\theta}_n^i + [D_{zz} - (nk_s)^2] \hat{\phi}_n^i, \tag{3.13}$$

$$[nk_s + g_n^i] \Delta^{\hat{\phi}_n} + [D_{zz} - (nk_s)^2 + h_n^i] \Delta^{\hat{\theta}_n} = \hat{f}_n^i, \tag{3.14}$$

where

$$\Delta^{\hat{\phi}_n} = \hat{\phi}_n^{i+1} - \hat{\phi}_n^i, \quad \Delta^{\hat{\theta}_n} = \hat{\theta}_n^{i+1} - \hat{\theta}_n^i, \tag{3.15a,b}$$

$D_{zz}$  is the second partial derivative operator with respect to  $z$ ,  $g_n^i$  and  $h_n^i$  can be obtained by calculating the convolution of the non-constant coefficient terms on the left-hand side of (3.11) for each iterate and  $\hat{f}_n^i$  represents the coefficients of the right-hand side of (3.11) in Fourier space at the  $i$ th iterate. We solve (3.13) and (3.14) numerically using a Chebyshev spectral collocation method.

Although the NK method is only locally convergent, the basin of attraction (in the space of initial iterates) can be expanded by updating the variables for each iterate using

$$\begin{bmatrix} \hat{\phi}_n \\ \hat{\theta}_n \end{bmatrix}^{i+1} = \begin{bmatrix} \hat{\phi}_n \\ \hat{\theta}_n \end{bmatrix}^i + a \begin{bmatrix} \Delta^{\hat{\phi}_n} \\ \Delta^{\hat{\theta}_n} \end{bmatrix}, \tag{3.16}$$

where  $0 \leq a \leq 1$ . The step-length coefficient  $a$  is reduced whenever  $F_{res}^{i+1} > b F_{res}^i$ , where  $F_{res}^i$  is the norm of the residual of the steady governing equations at the  $i$ th iterate and  $b \approx 1$  is an adjustable parameter. The iteration is continued until  $F_{res}^{i+1} < 10^{-7}$ , and then the spatial resolution is increased until the relative error in  $Nu$  is less than  $10^{-5}$ .

Computations are performed for a discrete set of  $Ra = 50 \times 10^{(j-1)/10}$  from  $Ra = 50$  to  $Ra = 31\,548$  and  $L_s = 0.01 \times 10^{(\hat{k}-1)/10}$  (for integer  $\hat{j}$  and  $\hat{k}$ ). For each  $Ra$ , we first solve the steady governing equations for a small aspect ratio  $L_s$  that is slightly greater than  $L_c$ , and then use that solution as the initial guess for a case with larger  $L_s$ .

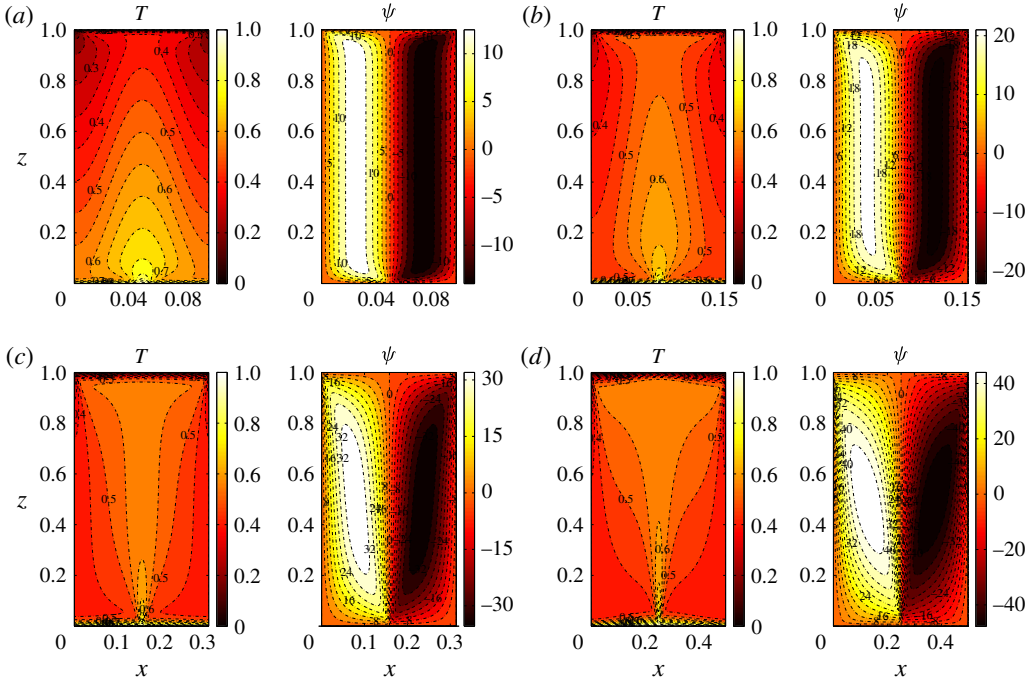


FIGURE 1. (Colour online) Temperature and stream function fields at  $Ra = 9976$  ( $L_c = 0.063$ ): (a)  $L_s = 0.1$ ; (b)  $L_s = 0.1585$ ; (c)  $L_s = 0.3162$ ; (d)  $L_s = 0.5012$ . The aspect ratio in (c) is close to the mean inter-plume spacing  $L_m = 0.319$  from DNS performed in a domain with  $L = 5.01$ . At small  $L_s$  (a,b) the interior streamlines are independent of  $z$ . However, as  $L_s$  is increased (c,d) the interior streamlines become  $z$ -dependent.

### 3.2. Solution structure

The structure of steady convection at large  $Ra$  depends on  $L_s$ . When  $L_s < L_c$ , the only steady solution is the conduction state. As  $L_s$  is increased, the conduction solution becomes linearly unstable, and two thin thermal boundary layers arise near the upper and lower walls (figure 1). Unlike the unsteady flow observed in DNS, the proto-plumes are absent in the steady solution. Near the walls there exists a boundary layer in the temperature field and a thicker boundary layer in the stream function field. Away from these nested boundary layers, the interior structure for small  $L_s$  is quite simple: the temperature deviation from the horizontal mean  $\theta' = T - \bar{T}$  and the stream function  $\psi$  are almost independent of  $z$ , so their  $z$ -derivatives are small (figure 1a,b; figure 2a,b), and there exists only a single non-zero horizontal Fourier mode (figure 2a,b). Indeed, this type of steady interior flow is well approximated using the analytical heat-exchanger solution

$$T(x, z) = \hat{T} \cos(kx) - \frac{k^2}{Ra} z + \left( \frac{k^2}{2Ra} + \frac{1}{2} \right), \tag{3.17}$$

$$w(x) = Ra \hat{T} \cos(kx), \tag{3.18}$$

$$u = 0 \tag{3.19}$$

given by Hewitt *et al.* (2012). This solution is obtained by balancing the vertical advection of a linearly varying interior mean temperature field  $\bar{T}$  with horizontal

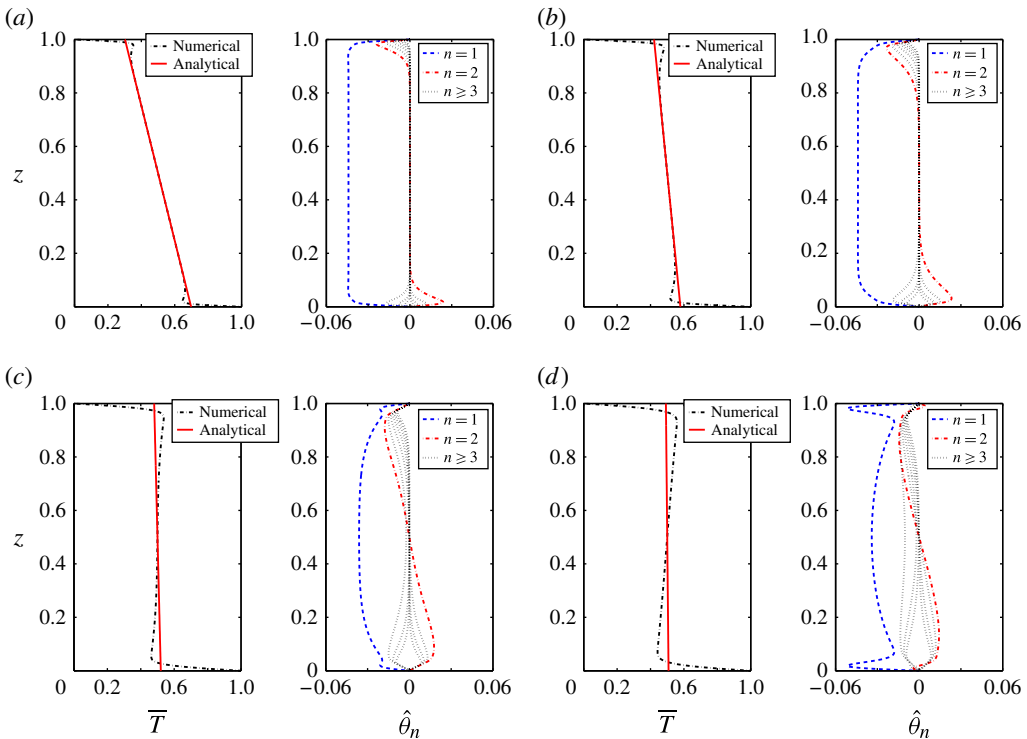


FIGURE 2. (Colour online) The  $z$ -dependent Fourier components of the temperature field for steady convective states at  $Ra = 9976$ : (a)  $L_s = 0.1$ ; (b)  $L_s = 0.1585$ ; (c)  $L_s = 0.3162$ ; (d)  $L_s = 0.5012$ . At small  $L_s$  ( $a, b$ ) the horizontal-mean temperature in the interior agrees closely with the analytical heat-exchanger solution; in the core, only a single (non-mean) Fourier mode is active and the temperature fluctuations are nearly independent of  $z$ . However, as  $L_s$  is increased ( $c, d$ ) more Fourier modes arise and the structure of the steady solutions departs from that of the analytical heat-exchanger solution even in the interior.

diffusion of temperature anomalies (with Fourier amplitude  $\hat{T}$ , which must be determined) between neighbouring mega-plumes. By comparing  $\bar{T}$  (figure 2*a, b*), the analytical heat exchanger and the steady-state numerical solutions are seen to agree closely. One significant difference, of course, is that the analytical heat-exchanger solutions do not satisfy the vertical boundary conditions. Therefore, we denote our numerically computed steady states at large  $Ra$  and small  $L_s$ , which not only exhibit the heat-exchanger structure in the interior but also satisfy the steady governing equations and all boundary conditions, as numerical heat-exchanger solutions.

Perhaps not surprisingly, as  $L_s$  is increased the steady large- $Ra$  numerical solutions do not retain the heat-exchanger structure in the interior. Instead, the streamlines deviate from the vertical (figure 1*c, d*), and multiple horizontal Fourier modes are excited, although the fundamental mode still dominates the flow (figure 2*c, d*). Moreover, when  $L_s$  is sufficiently large, the numerically computed  $\bar{T}$  clearly deviates from that predicted by the heat-exchanger solution. In fact, the slope of  $\bar{T}$  at the mid-plane  $z = 0.5$  becomes positive, implying that hotter fluid overlies colder fluid in the interior. We refer to this class of numerically computed steady states as stably stratified core solutions.

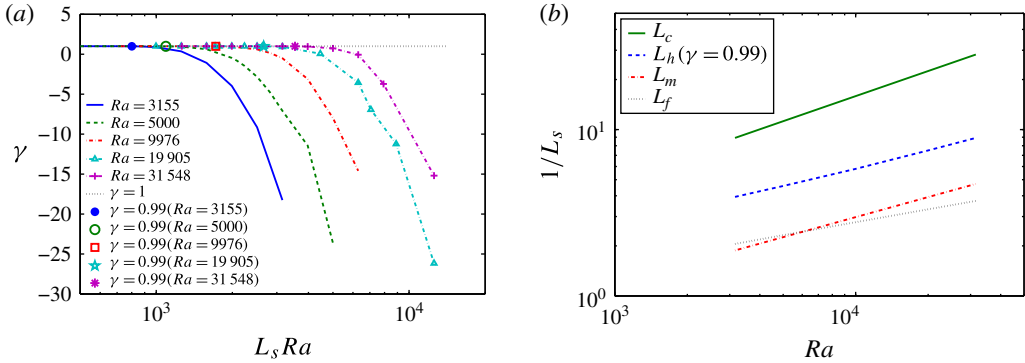


FIGURE 3. (Colour online) (a) Proximity of numerical solutions to the heat-exchanger solution:  $\gamma = -(Ra/k_s^2)\partial_z \bar{T}|_{z=0.5}$  versus  $L_s Ra$ . As  $L_s$  is increased,  $\gamma$  eventually departs from unity and the interior structure of the numerical solution changes from that of the heat-exchanger solution to that of the stably stratified core solution. (b) Variation with  $Ra$  of  $L_h$ , the wavelength of steady solutions with  $\gamma = 0.99$  (i.e. numerical heat-exchanger solutions). Also plotted for comparison are  $L_c \sim 2\pi Ra^{-0.5}$ , the wavelength of the marginal stability boundary,  $L_m \approx (2\pi/0.47)Ra^{-0.4}$ , the mean inter-plume spacing measured from the DNS of Hewitt *et al.* (2012), and  $L_f \sim 2\sqrt{\pi}Ra^{-0.25}$ , the wavelength of the fastest-growing linear mode. Interestingly, at large  $Ra$ ,  $L_m \approx 2L_h$ .

To quantify the proximity of a given numerically computed steady solution to the analytical heat-exchanger solution in the interior we introduce the parameter

$$\gamma = -\frac{Ra}{k_s^2}\partial_z \bar{T}|_{z=0.5} \tag{3.20}$$

measuring the ratio of the numerically computed mean temperature gradient at the mid-plane to the analytically predicted (constant) vertical temperature gradient. The solutions are identical when  $\gamma = 1$ , and so we quantitatively (but arbitrarily) define the steady convective state as a numerical heat-exchanger solution when  $0.99 \leq \gamma \leq 1$ .

Figure 3 shows how the structure of the steady solution changes as  $Ra$  and  $L_s$  are varied. For small  $L_s > L_c$ , we observe that  $0.99 \leq \gamma \leq 1$ , so these solutions belong to the class of numerical heat-exchanger solutions. However,  $\gamma$  decreases appreciably as  $L_s$  increases, and the steady solutions assume a transitional form for  $0 < \gamma < 0.99$ . When  $L_s$  is sufficiently large,  $\gamma$  changes sign, yielding a family of stably stratified core solutions. It should be noted that the wavelength  $L_h$  of solutions with  $\gamma = 0.99$  (see figure 3b), which separates the heat-exchanger and non-heat-exchanger solutions, is approximately half the mean inter-plume spacing ( $L_m$  in figure 3b) measured from the DNS of Hewitt *et al.* (2012).

### 3.3. Maximising $Nu$

Of particular physical importance is the relationship between the Nusselt number  $Nu$  and the two control parameters  $Ra$  and  $L$ . Wen *et al.* (2013) systematically studied the influence of the domain aspect ratio on the heat transport in turbulent porous medium convection using upper bound theory and DNS. At large  $Ra$  the turbulent flow in porous medium convection was found to be self-sustaining with a  $Ra$ -dependent



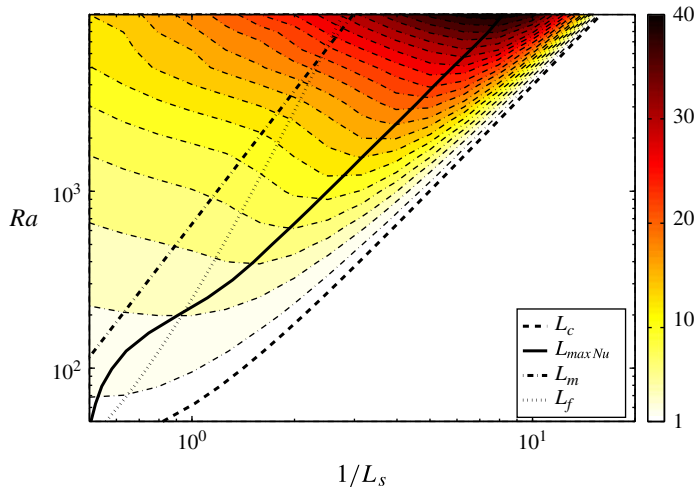


FIGURE 4. (Colour online) Contour plot of the Nusselt number in  $(Ra, L_s)$  parameter space for steady convective states. The solid line ( $L_{maxNu}$ ) marks the path along which  $Nu$  is maximised. Here,  $L_c$ ,  $L_m$  and  $L_f$  are as in figure 3.

lateral scale, identified as a ‘minimal flow unit’, above which the heat transport is effectively independent of  $L$ . The dependence of  $Nu$  on  $Ra$  and  $L_s$  in steady porous medium convection, however, differs both qualitatively and quantitatively from that characterising turbulent heat transport in a porous layer. Figure 4 shows the variation of  $Nu$  with  $Ra$  and  $L_s$  for steady convective states (see also Corson 2011). There is no convection when the domain aspect ratio is smaller than the wavelength  $L_c$  of the marginal stability mode, so  $Nu = 1$  in this regime. Unlike time-dependent convection, for which the value of  $Nu$  asymptotes when the domain aspect ratio exceeds the size of the minimal flow unit, the heat transport in steady convection is maximised along a particular path in  $(Ra, L_s)$  parameter space (the solid black curve in figure 4).

To accurately extract the scalings associated with the steady heat-flux-maximising solutions, we employed greater resolution in parameter space for  $(Ra, L_s)$  pairs near the ridge along which  $Nu$  is maximised. We also continued the computations to  $Ra = 31\,548$ , as shown in figures 4 and 5. When  $Nu$  is maximum and  $Ra$  is less than roughly 100,  $L_s$  scales as  $Ra^{-1/4}$ , the scaling for the wavelength  $L_f$  of the fastest-growing linear mode. As  $Ra$  is increased, the ridge of maximum  $Nu$  shifts to the right and for  $10^3 < Ra < 10^4$ ,  $L_s \sim Ra^{-0.52}$ . As is evident in figure 5(a), the heat-flux-maximising solutions at large  $Ra$  are, in fact, numerical heat-exchanger states. Figure 5(b) shows the variation of  $Nu$  with  $Ra$  for high- $Ra$  steady solutions on the ridge (Corson 2011), along with results from upper bound analysis and DNS. Both the upper bound calculation and the DNS predict  $Nu \sim Ra$  for the unsteady flow. Steady convection at large  $Ra$  is thus seen to transport less heat than the realised turbulent flow, with  $Nu \sim Ra^{0.6}$  for the equilibrium states (Corson 2011). Like the real flow, however, the heat transported by the steady heat-flux-maximising solutions increases substantially as the inter-plume spacing (i.e.  $L_s$ ) decreases from  $O(1)$  to asymptotically small values; in contrast, the matched asymptotic analysis of Fowler (1997) suggests that in steady porous medium convection at fixed aspect ratio  $Nu \sim Ra^{1/3} = o(Ra^{0.6})$ .

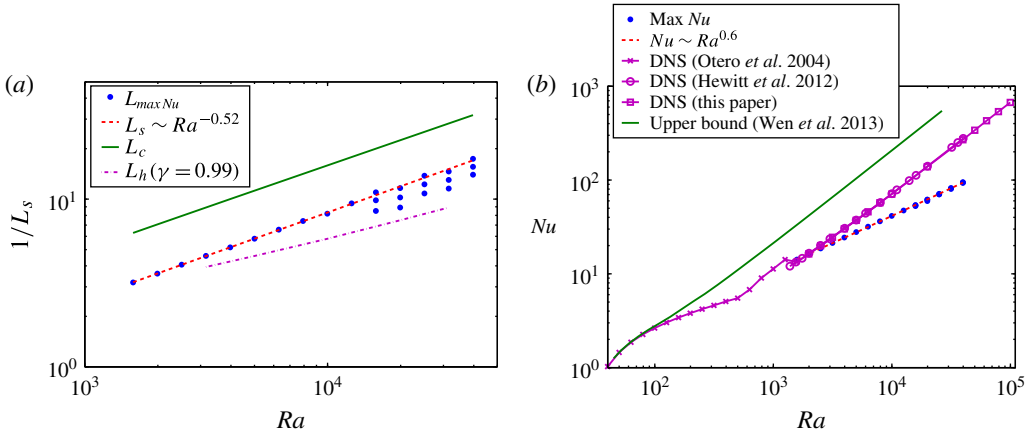


FIGURE 5. (Colour online) (a) Rayleigh-number scaling of the inverse wavelength associated with heat-flux-maximising steady convective states (dots). It should be noted that at sufficiently large  $Ra$  multiple states yield nearly the same (maximum) heat flux. The dashed line is the best fit curve  $1/L_s = 0.070Ra^{0.52}$  for  $Ra \leq 12\,559$ . For reference,  $1/L_h$  and  $1/L_c$  are also plotted as functions of  $Ra$ . (b) Rayleigh-number scaling of the Nusselt number for steady convective solutions (dots). The dashed line is the best fit curve  $Nu = 0.155Ra^{0.60} + 1.213$ . For reference, data from upper bound analysis and various DNS are also shown.

### 3.4. Statistical structure of the columnar flow in DNS

As described above, the spatial structure of steady convection varies appreciably with  $L_s$ . A natural question concerns the difference between the structure of the steady convective states and that of the time-averaged flow observed in DNS. As  $Ra$  increases, DNS indicate that the interior flow becomes more organised and is dominated by persistent vertical columnar flow across the domain, driven by the chaotic mixing of small proto-plumes at the upper and lower boundaries (Otero *et al.* 2004; Hewitt *et al.* 2012). The columnar flow has been modelled using the heat-exchanger solution in Hewitt *et al.* (2012, 2013). As discussed in § 3.2, the heat-exchanger solution is well represented by the interior part of steady solutions only for convective states with sufficiently small aspect ratios; of course, the time-averaged columnar flow in DNS need not satisfy the steady governing equations. To further investigate the differences between the time-averaged columnar flow and the strictly steady convective states, we performed DNS in the high- $Ra$  regime, extending previous results to  $Ra \approx 10^5$ . The unsteady version of the system (3.1) and (3.2) was solved numerically using a Fourier–Chebyshev- $\tau$  pseudospectral algorithm. Temporal discretisation was achieved using the Crank–Nicolson method for the linear terms and a two-step Adams–Bashforth method for the nonlinear terms, yielding second-order accuracy in time. The code was thoroughly validated and gives  $Nu$  values quantitatively matching those of previous DNS, as shown in figure 5(b).

Figure 6 shows snapshots of the temperature fields and corresponding long-time-averaged magnitudes of the (complex) Fourier amplitudes of the temperature fluctuations (i.e. deviations from the horizontal mean) as functions of  $z$  from our DNS at  $Ra = 50\,000$  conducted in two different domains. As is evident in figure 6(a), there exist 17 very well organised columnar flows, each consisting of a single rising and descending mega-plume, at the given parameter values. The time-averaged amplitudes

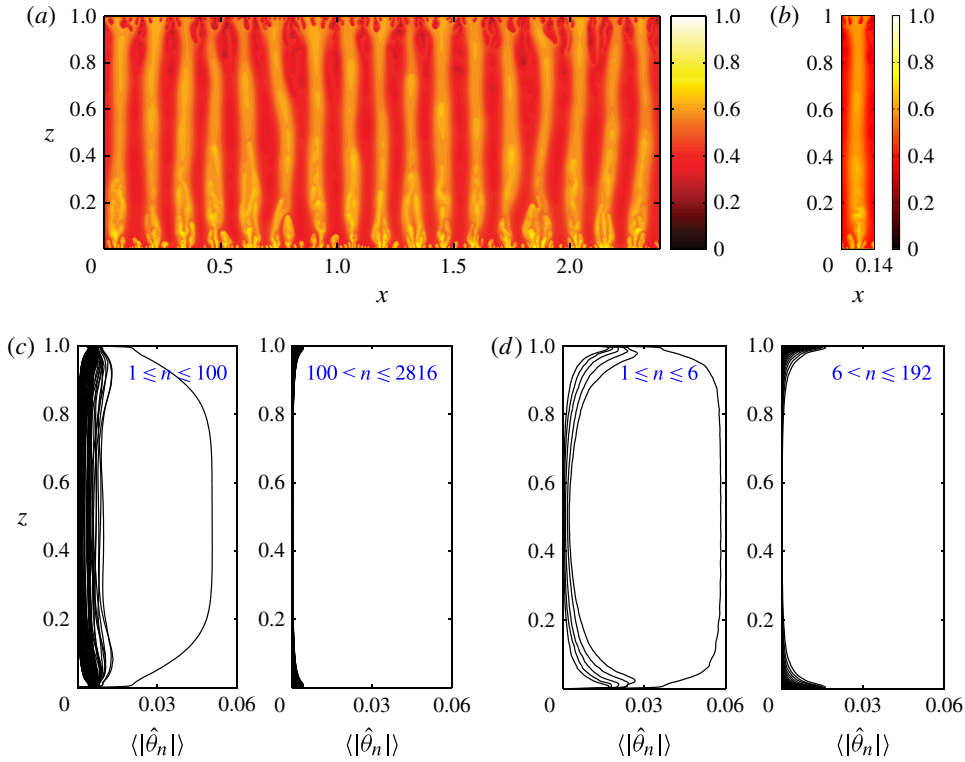


FIGURE 6. (Colour online) Snapshots of the temperature fields (*a,b*) and corresponding time-averaged Fourier amplitudes (*c,d*) of the temperature fluctuations (i.e. deviations from the horizontal mean) from DNS at  $Ra = 50\,000$ . In (*a,c*)  $L = 2.39$ , while in (*b,d*)  $L = 2.39/17$ .

of the temperature fluctuations,  $\langle |\hat{\theta}_n| \rangle$ , in figure 6(*c*) reveal that the interior flow is a composite of a few low-wavenumber Fourier modes but is dominated by one mode, features shared by the strictly steady stably stratified core solutions. Indeed, we recall that steady convective states with  $L_s = L_m$ , the mean inter-plume spacing observed in DNS, are stably stratified core solutions (figures 1*c*, 2*c* and 3*b*). Furthermore, at high wavenumber, the Fourier amplitudes  $\hat{\theta}_n$  are strongly localised near the upper and lower walls, where they superpose to comprise the small rolls and proto-plumes within the thermal and vorticity boundary layers. Figure 6(*b,d*) shows corresponding results for DNS performed in a narrower domain, confirming that the flow has a structure similar to that in the larger domain. In particular, the time-averaged interior flow is well represented by only six Fourier modes.

Nevertheless, the DNS indicate that the interior slope of the time- and horizontal-mean temperature field is not positive (figure 7*a*); i.e. the core is not stably stratified. Furthermore, although the interior mean temperature profile is roughly linear in  $z$  with negative slope for large  $Ra$ , this slope is not well predicted by the heat-exchanger solution either: compared with the slope of  $\bar{T}$  for the heat-exchanger solution, the mean temperature gradient from the DNS is more negative (figure 7*a*). On the other hand, figure 7 does confirm that the mean temperature gradient approaches zero as  $Ra$  is increased and that the mean amplitude of the dominant Fourier mode in the interior is almost independent of  $Ra$  at large  $Ra$  (figure 7*b*), consistent with the measurements

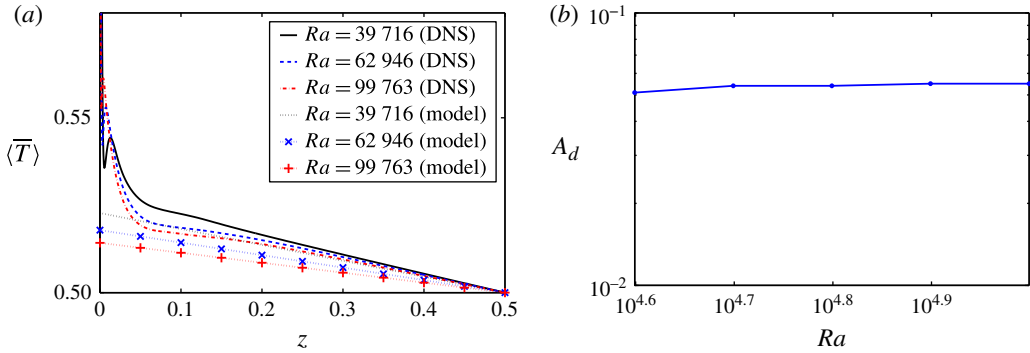


FIGURE 7. (Colour online) Statistical structure of turbulent convection obtained from DNS. (a) Comparison of the long-time- and horizontally averaged temperature profile  $\langle \bar{T} \rangle$  from DNS with  $\bar{T}$  from the analytical heat-exchanger model. (b) Time-averaged amplitude  $A_d$  of the dominant Fourier mode (after subtraction of the horizontal mean) at  $z = 0.5$ . For each  $Ra$ , DNS was performed in a domain with  $L = 10L_f$  so that 17 columnar flows were captured. In (a), only half of the mean temperature profile (i.e. for  $0 \leq z \leq 0.5$ ) is plotted due to statistical antisymmetry about the mid-plane.

in Hewitt *et al.* (2012) and the form of the heat-exchanger solution. In short, the statistical structure of the turbulent columnar flow at large  $Ra$  resembles the heat-exchanger solution in the interior, but with a modified mean temperature gradient and more than one Fourier mode to adequately represent the fluctuations.

#### 4. Secondary stability analysis

##### 4.1. Floquet theory

To investigate the stability properties of the steady convective states described in the previous section, we next perform a secondary stability analysis using spatial Floquet theory. First, all fields are expressed as the sum of the steady nonlinear base flow (denoted with a subscript ‘s’) and a time-varying perturbation,

$$T(x, z, t) = T_s(x, z) + \tilde{\theta}(x, z, t), \tag{4.1}$$

$$\psi(x, z, t) = \psi_s(x, z) + \tilde{\psi}(x, z, t), \tag{4.2}$$

where  $T_s = (1 - z) + \theta_s$ . Then the equations governing the evolution of the presumed small-amplitude disturbances can be expressed as

$$\nabla^2 \tilde{\psi} = -Ra \partial_x \tilde{\theta}, \tag{4.3}$$

$$\partial_t \tilde{\theta} = \nabla^2 \tilde{\theta} - \partial_x \theta_s \partial_z \tilde{\psi} + \partial_z \theta_s \partial_x \tilde{\psi} + \partial_x \psi_s \partial_z \tilde{\theta} - \partial_z \psi_s \partial_x \tilde{\theta} - \partial_x \tilde{\psi}, \tag{4.4}$$

where the perturbation fields also satisfy the boundary conditions

$$\tilde{\theta}(x, 0, t) = 0, \quad \tilde{\theta}(x, 1, t) = 0, \quad \tilde{\psi}(x, 0, t) = 0, \quad \tilde{\psi}(x, 1, t) = 0 \tag{4.5a-d}$$

and  $L$ -periodicity (not generally  $L_s$ -periodicity) in  $x$ . Floquet theory implies that solutions may be sought having the following form:

$$\begin{bmatrix} \tilde{\theta} \\ \tilde{\psi} \end{bmatrix} = e^{i\beta k_s x} \left\{ \sum_{n=-\infty}^{\infty} \begin{bmatrix} \hat{\theta}_n(z) \\ \hat{\psi}_n(z) \end{bmatrix} e^{ink_s x} \right\} e^{\lambda t} + \text{c.c.}, \tag{4.6}$$

where  $\lambda$  is the temporal growth rate,  $i\beta k_s$  is the Floquet exponent, with the real Floquet parameter  $\beta$  providing the freedom to modify the fundamental horizontal wavenumber of the perturbation (i.e. for  $\beta \neq 0$ ,  $\beta k_s$  is the wavenumber of the largest horizontal scale), and c.c. denotes complex conjugate. Since (4.6) is invariant under integer shifts in  $\beta$  and under reflections  $\beta \rightarrow -\beta$ , we can restrict attention to  $0 \leq \beta \leq 0.5$  without loss of generality. Substitution of (4.6) into (4.3) and (4.4) yields

$$i(n + \beta)k Ra \hat{\theta}_n + [D_{zz} - (n + \beta)^2 k^2] \hat{\psi}_n = 0, \tag{4.7}$$

$$[D_{zz} - (n + \beta)^2 k^2 + \tilde{h}_n] \hat{\theta}_n + [-i(n + \beta)k + \tilde{g}_n] \hat{\psi}_n = \lambda \hat{\theta}_n \tag{4.8}$$

for each  $n$ , where  $\tilde{h}_n$  and  $\tilde{g}_n$  can be determined by calculating the convolution of the non-constant-coefficient terms in (4.4). After setting  $\hat{\psi}_n = i \hat{\phi}_n$ , (4.7) and (4.8) can be written in the form

$$\mathbf{A}\mathbf{V} = \lambda \mathbf{B}\mathbf{V}, \tag{4.9}$$

where  $\mathbf{A}$  and  $\mathbf{B}$  are real matrices due to the symmetries (3.4) of the base flow, and the vector  $\mathbf{V} = (\dots \hat{\theta}_{n-1}, \hat{\theta}_n, \hat{\theta}_{n+1} \dots \hat{\phi}_{n-1}, \hat{\phi}_n, \hat{\phi}_{n+1} \dots)^T$ . The eigenvalue  $\lambda$  and the corresponding eigenvector  $\mathbf{V}$  can be obtained by numerically solving this differential eigenvalue problem. It should be noted that in the following sections, the convective rather than diffusive time,  $\tau \equiv tRa$ , will be utilised, so that the corresponding convective growth rate  $\sigma \equiv \lambda/Ra$ .

### 4.2. Secondary stability results

The eigensystem (4.9) is discretised using a Chebyshev collocation method and the infinite-dimensional system is truncated to  $0 \leq m \leq M$  vertically and  $-N/2 \leq n \leq N/2$  horizontally. Arnoldi iteration is used to solve the resulting algebraic eigenvalue problem to obtain the leading eigenvalues and eigenfunctions. The numerical resolution is increased until the relative error in the eigenvalue with the largest real part,  $\sigma_m$ , is less than  $10^{-4}$ .

Figure 8 shows the contours of maximum growth rate,  $\text{Re}\{\sigma_m\}$ , as a function of  $\beta$  and  $L_s$  for various  $Ra$ . At a given  $Ra$ , the steady solution at small  $L_s$  (specifically,  $L_c < L_s < L_b$ , where  $L_b$  is a stability boundary defined in figures 10 and 11) is marginally stable for  $\beta = 0$  – corresponding to disturbances that simply translate the steady base flow in  $x$  – although there is insufficient resolution around  $\beta = 0$  to observe this clearly in the contour plots. However, the solution is unstable for a range of long-wavelength perturbations ( $0 < \beta \leq 0.5$ , see figure 8). The Floquet parameter  $\beta$  of the fastest-growing perturbation is approximately 0.2–0.3, implying that the most unstable disturbance has a wavelength 3–5 times the wavelength of the base flow. At  $Ra = 1581$  and 3155, the growth rate of the most unstable mode decreases as  $L_s$  is increased and, in fact, the steady solution becomes linearly stable for a finite range of  $L_s$ . However, as  $L_s$  is further increased, the steady state becomes unstable, exhibiting a growth rate that is essentially independent of  $\beta$ . Similar phenomena are observed at larger  $Ra$  except that the linearly stable region shrinks nearly to a point at  $Ra = 5000$  and vanishes completely at larger  $Ra$ .

Figure 9 shows, for  $Ra = 9976$ , the 2D eigenfunctions corresponding to these two families of secondary instabilities. At small  $L_s$ , e.g.  $L_s = 0.1$ , when the growth rate depends on the horizontal wavenumber  $\beta k_s$ , the most unstable perturbation (occurring for  $\beta \approx 0.2$ ) is a bulk mode that spans the layer (figure 9a). However,

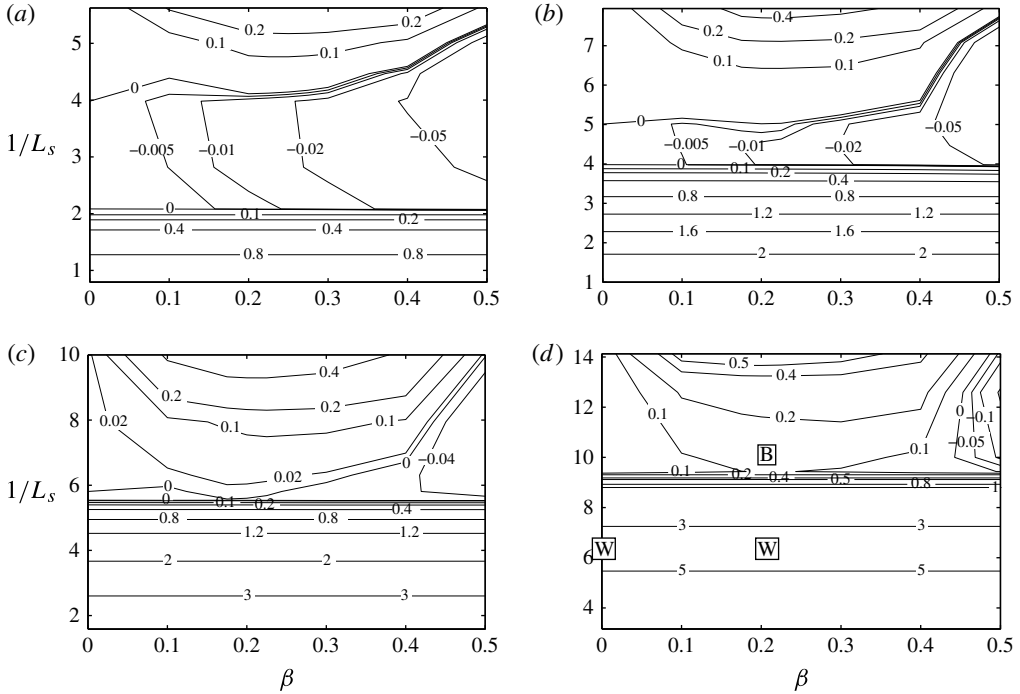


FIGURE 8. Contours of the maximum growth rate  $\text{Re}\{\sigma_m\}$  as a function of  $\beta$  and  $L_s$  for various  $Ra$ : (a)  $Ra = 1581$ ; (b)  $Ra = 3155$ ; (c)  $Ra = 5000$ ; (d)  $Ra = 9976$ . At small  $L_s$  ( $L_c < L_s < L_b$ ), the base state is stable within small domains of size  $L_s \times 1$  (since  $L = L_s$  for  $\beta = 0$ ), but unstable to certain long-wavelength perturbations ( $0 < \beta \leq 0.5$ ); at large  $L_s$ , the base state is unstable even for  $\beta = 0$ , and has the same growth rate for different  $\beta$ . It should be noted that the contour plot in (d) has been annotated to indicate the parameters corresponding to the bulk ('B') and wall ('W') mode eigenfunctions displayed in figure 9.

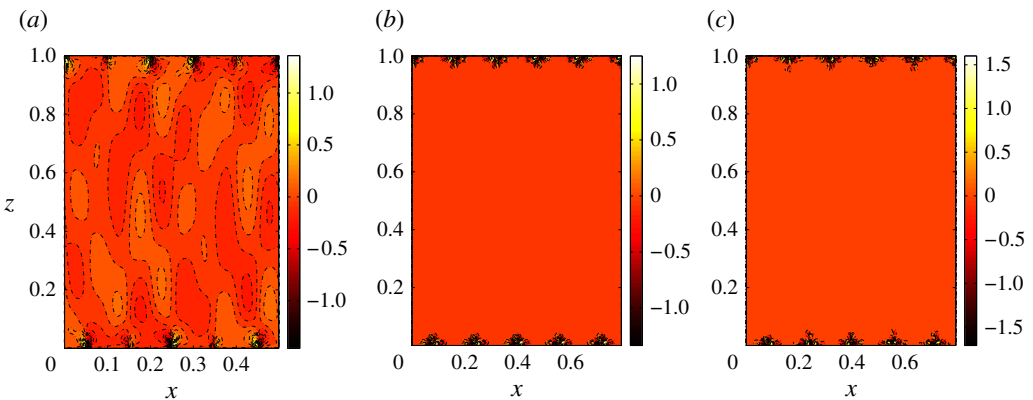


FIGURE 9. (Colour online) The fastest-growing 2D temperature eigenfunctions at  $Ra = 9976$  shown in a domain with aspect ratio  $L = 5L_s$  (where  $L_s$  is the wavelength of the steady base state): (a)  $L_s = 0.1$ ,  $\beta = 0.2$ ; (b)  $L_s = 0.1585$ ,  $\beta = 0$ ; (c)  $L_s = 0.1585$ ,  $\beta = 0.2$ . At small  $L_s$ , a bulk mode controls the instability, and at large  $L_s$ , a wall mode dominates. It should be noted that at large  $L_s$  the spatial structure of the fastest-growing (wall) mode is nearly independent of  $\beta$ .



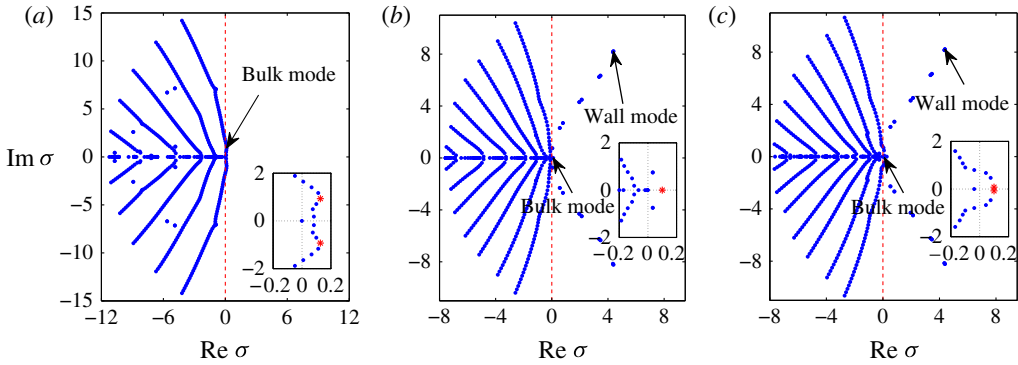


FIGURE 10. (Colour online) The leading eigenvalues at  $Ra = 9976$ : (a)  $L_s = 0.1$ ,  $\beta = 0.2$ ; (b)  $L_s = 0.1585$ ,  $\beta = 0$ ; (c)  $L_s = 0.1585$ ,  $\beta = 0.2$ ;  $\text{Re } \sigma$  ( $\text{Im } \sigma$ ) is the real (imaginary) part of  $\sigma$ . In each case, the inset shows a magnification of the region near the origin, with the asterisk denoting the most unstable bulk mode(s). Here,  $L_b$  is defined such that when  $L_s < L_b$  (as in a) only bulk modes exist. As  $L_s$  is increased (b,c), an increasing number of wall modes are destabilised. One should note the similarity of the eigenspectra in (b) and (c) for the same (large)  $L_s$ .

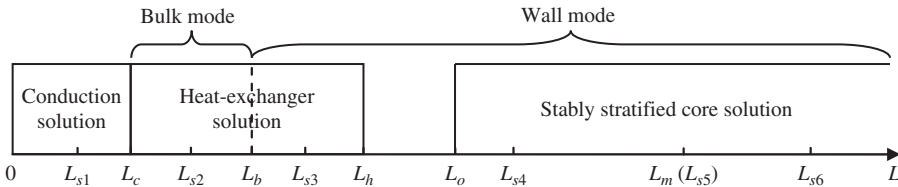


FIGURE 11. Schematic identifying distinct steady states and the associated secondary instability regimes at large  $Ra$ . DNS are performed for six steady base states with aspect ratios  $L_{s1} - L_{s6}$  to study the fully nonlinear evolution of the fastest-growing instability modes. Here,  $L_o$  is the aspect ratio for which the normalised horizontal-mean temperature gradient  $\gamma = 0$ .

for larger  $L_s$ , e.g.  $L_s = 0.1585$ , the most unstable perturbation for each  $\beta$  has nearly the same growth rate and a very similar spatial structure, which is strongly localised near the upper and lower walls (figure 9b,c). Figure 10 shows the eigenspectrum for three different ( $\beta, L_s$ ) combinations. We note that the bulk mode, as shown in figure 9(a), occurs for certain long-wavelength (e.g.  $\beta = 0.2$ ) disturbances and exhibits comparably small growth rates ( $\sigma_m = O(0.1)$ ). At small  $L_s$ , the bulk modes control the instability. As  $L_s$  is increased, however, an increasing number of wall modes become unstable. These wall modes, which are born in a Hopf bifurcation associated with the advection of small-scale disturbances within the thermal boundary layers (see Aidun & Steen (1987) and Graham & Steen (1992, 1994)), ultimately dominate the secondary instability with growth rates 10–50 times larger than those associated with the bulk modes. For sufficiently large  $L_s$ , the eigenspectra for disturbances with distinct fundamental horizontal wavenumbers are very similar. We conclude this section by contrasting our secondary stability results with those of Hewitt *et al.* (2013). Not only do we find two modes of instability rather than one, but in the presence of walls the bulk modes are found to have much reduced growth rates: specifically,  $O(0.1)$  rather than  $O(1)$ .

## 5. Nonlinear evolution of the instability

In this section we use strategically initialised high-resolution DNS in wide domains to investigate the nonlinear evolution of the fastest-growing secondary instability mode for various steady convective states distinguished by their wavelength  $L_s$ . Our aim is to gain insight into the mechanisms by which the base flow, with plume spacing  $L_s$ , evolves to the final columnar flow, with mean inter-plume spacing  $L_m$  (in the bulk). The steady state at a given  $L_s$  plus a small-amplitude contribution of the most unstable secondary instability mode is chosen as the initial condition, and then DNS is performed in a large domain with  $L = 10L_s - 20L_s$ .

As shown in figure 11, for a specific large  $Ra = O(10^4)$ , with increasing  $L$ , generally  $L_c < L_b < L_{maxNu} < L_h < L_o < L_m$ , where  $L_c$  is the wavelength of the neutral mode on the right-hand marginal stability boundary of the conduction state,  $L_b$  is the largest aspect ratio at which only the bulk instability mode exists,  $L_{maxNu}$  is the wavelength of the steady cellular flow that maximises the heat transport,  $L_h$  is the largest aspect ratio at which the heat-exchanger solution is relevant and  $L_o$  is the aspect ratio at which the parameter  $\gamma$  vanishes (implying a steady base flow with zero mean stratification in the centre of the cell). In the following sections, six different steady convective states, five at  $Ra = 9976$  and one at  $Ra = 50\,000$ , are considered:  $L_{s1}$  is less than  $L_c$  so that the base state is the conduction solution;  $L_{s2}$  is greater than  $L_c$  but within the aspect-ratio range for which the bulk mode controls the instability;  $L_{s3}$  is greater than  $L_b$  but is within the numerical heat-exchanger solution regime;  $L_{s4}$  is between  $L_h$  and  $L_m$ , within the stably stratified core solution regime;  $L_{s5}$  is close to the final mean inter-plume spacing  $L_m$ ; and  $L_{s6}$  is much larger than  $L_m$ . Thus, for  $Ra = 9976$ , for example,  $L_c = 0.063$ ,  $L_b = 0.106$ ,  $L_h = 0.172$ ,  $L_m = 0.319$  (measured from DNS in  $L = 5.012$ ) and  $L_f = 0.36$ .

### 5.1. $L_{s2}$ ( $Ra = 9976$ )

For  $Ra = 9976$ , we first perform DNS to investigate the dynamics ensuing from unstable steady states with  $L_s = L_{s2}$ , which is within the bulk instability parameter regime. The initial condition comprises 20 replicas of the steady convective state at  $L_s = 0.1$  plus a small-amplitude contribution of the corresponding fastest-growing perturbation at  $\beta = 0.2$ . Figure 12 depicts the nonlinear evolution from this initial state to the final turbulent columnar flow. Initially, the dominant horizontal mode number in the interior is  $n_d = 20$ . In accord with the stability analysis in § 4 and as is evident in figure 12(b,c), the base state is unstable to a bulk mode. As the secondary mode grows in amplitude, the pattern coarsens to an unsteady convective state at  $\tau = 87.29$  (figure 12d) with five times the wavelength of the initial steady cellular solution. The resulting mean inter-plume spacing, however, is larger than the final  $L_m$ . Subsequently, some plumes growing from the upper and lower boundary layers split the wider plumes into narrower ones (figure 12e). These proto-plumes appear to be generated by a localised instability that closely resembles the wall-mode secondary instability of strictly steady base states having a wavelength greater than  $L_b$  (figure 12d). Ultimately, the system converges to a statistically steady turbulent state (figure 12f). Thus, there exist two stages of evolution: initially, the bulk instability controls the evolution of the flow so that the background plumes merge forming a convective flow with smaller interior wavenumber; then, as the plume spacing becomes too wide, a variant of the boundary instability intensifies so that small plumes generated from the upper and lower walls are able to split the wider plumes into narrower ones until the flow settles into a statistically steady state. We note

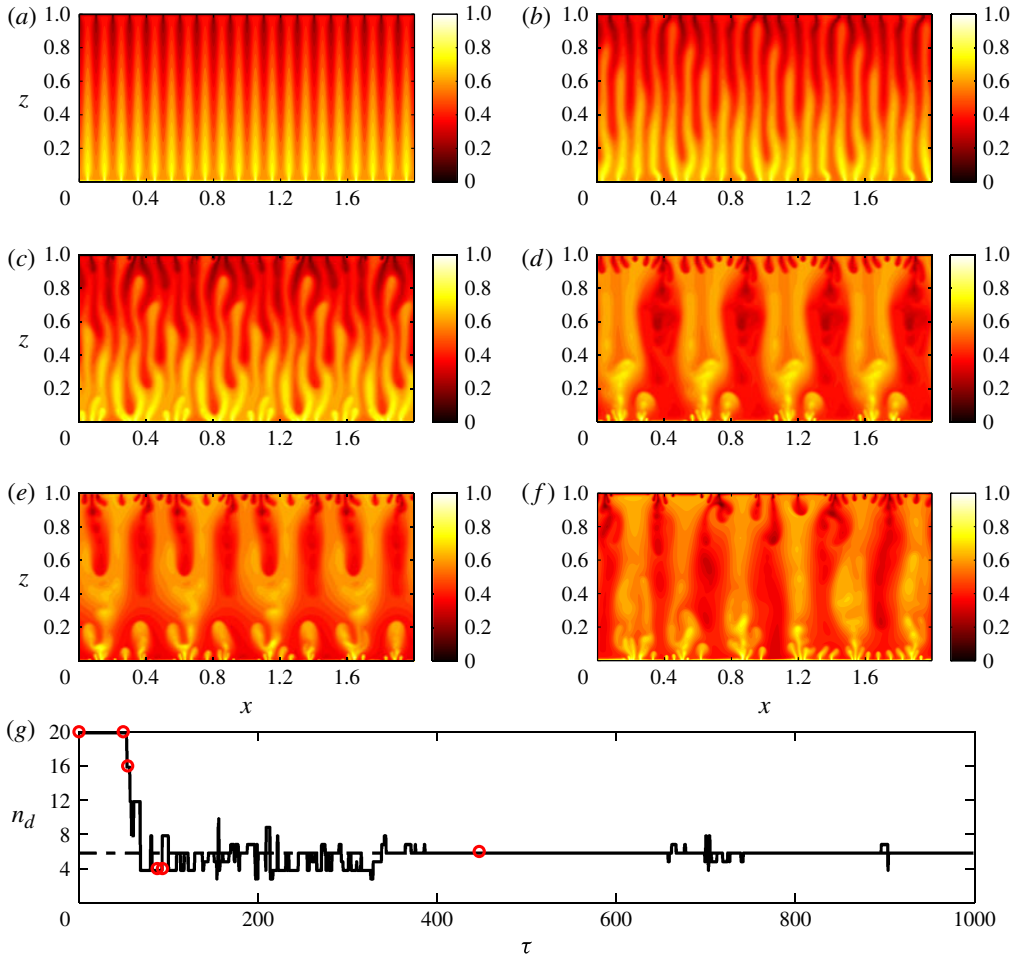


FIGURE 12. (Colour online) Snapshots of the temperature field from DNS showing the nonlinear evolution of the fastest-growing secondary instability mode for  $L_{s2} = 0.1$ ,  $L = 20L_{s2}$ ,  $Ra = 9976$ : (a)  $\tau = 0$ ; (b)  $\tau = 49.38$ ; (c)  $\tau = 54.37$ ; (d)  $\tau = 87.29$ ; (e)  $\tau = 93.28$ ; (f)  $\tau = 446.94$ . (g) The time evolution of the dominant horizontal mode number  $n_d$  at  $z = 0.5$  (solid line). The dashed line shows the time-average dominant mode number and the circles correspond to the times highlighted in (a–f).

that the first stage of this process is loosely similar to the instability and predicted nonlinear evolution of the analytical heat-exchanger flow described in Hewitt *et al.* (2013), in which only the bulk instability mode is found.

### 5.2. $L_{s3}$ ( $Ra = 9976$ )

Next, we consider a wider base flow with  $L_s = L_{s3} = 0.1585$ , which also is a member of the numerical heat-exchanger family but which is (most) unstable to wall modes. From the stability analysis, the growth rate and spatial structure of the most unstable perturbation are nearly independent of  $\beta$  (figures 8d and 9b,c). The initial condition for the DNS consists of 16 copies of this steady state plus a small-amplitude contribution of the most unstable perturbation at  $\beta = 0$ . Figure 13 shows the nonlinear

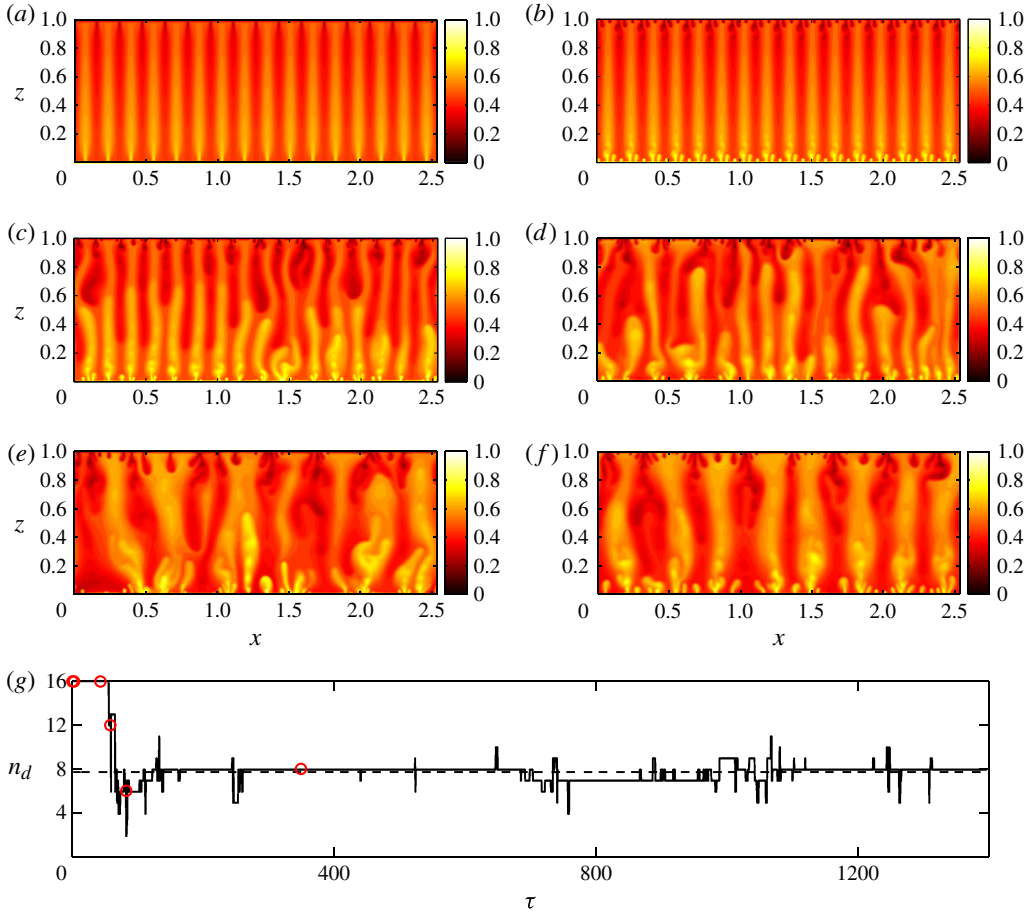


FIGURE 13. (Colour online) Snapshots of the temperature field from DNS showing the nonlinear evolution of the fastest-growing secondary instability mode for  $L_{s3} = 0.1585$ ,  $L = 16L_{s3}$ ,  $Ra = 9976$ : (a)  $\tau = 0$ ; (b)  $\tau = 2.49$ ; (c)  $\tau = 42.90$ ; (d)  $\tau = 57.86$ ; (e)  $\tau = 82.30$ ; (f)  $\tau = 349.17$ . (g) The time evolution of the dominant horizontal mode number  $n_d$  at  $z = 0.5$  (solid line). The dashed line shows the time-average dominant mode number and the circles correspond to the times highlighted in (a–f).

evolution from this initial condition to the final state. By construction, the dominant horizontal mode number in the interior is  $n_d = 16$  at  $\tau = 0$ . At early times ( $\tau = 2.49$ , figure 13b), proto-plumes generated in the upper and lower boundary layers because of the wall instability are continually swept into and thus merge with the mega-plumes in the interior. However, the resulting quasi-time-periodic flow itself evidently is unstable to a variant of the bulk mode (figure 13c), causing a coarsening of the convective pattern (figure 13d,e), in rough correspondence with the first stage of the evolution for the base flow with  $L_s = L_{s2}$ . The plumes generated from the walls then split the wider plumes before the flow reaches a statistically steady state (figure 13f), similar to the second stage of the evolution for the case for which  $L_s = L_{s2}$ . Interestingly, the final state is not dominated by a unique horizontal wavenumber in the interior. In short, there exist three evolutionary stages for the scenario with  $L_s = L_{s3}$ . In the linear instability regime, the wall mode dominates the evolution of the flow so that a

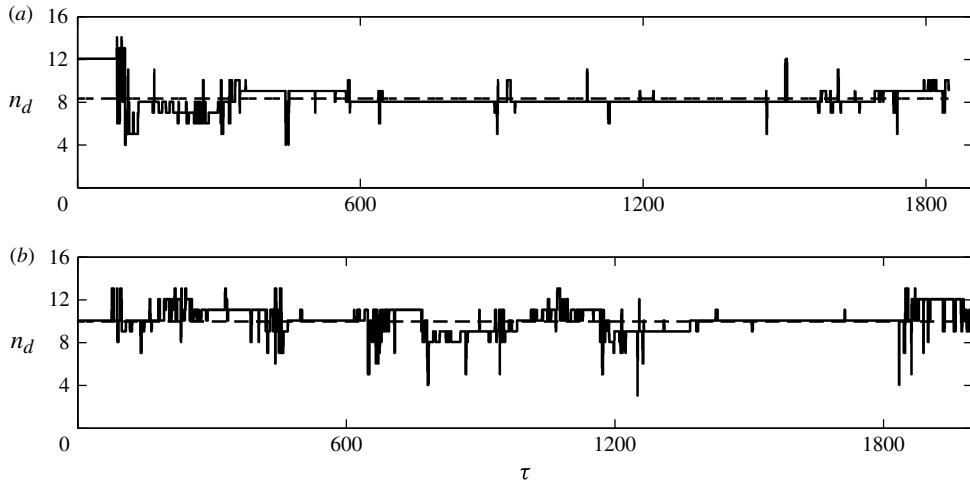


FIGURE 14. The time evolution of the dominant horizontal mode number  $n_d$  at  $z = 0.5$  for the temperature field from DNS at  $Ra = 9976$  (solid line); the dashed line shows the time-average dominant mode number: (a)  $L_{s4} = 0.224$ ,  $L = 12L_{s4}$ ; (b)  $L_{s5} = 0.316$ ,  $L = 10L_{s5}$ .

series of proto-plumes rising from the walls merge with the background mega-plumes; this process leaves the mean inter-plume spacing unchanged from its initial value  $L_s$ . However, the modified roughly time-periodic flow appears to be susceptible to a bulk instability, causing the merger of some mega-plumes. Finally, as the inter-plume spacing increases, a wall-like mode is again activated and some of the nascent proto-plumes split the wider plumes, yielding the final turbulent convective state. This scenario suggests that a generalisation of the bulk instability may occur for unsteady flow, and that this instability intensifies as the inter-plume spacing is reduced.

### 5.3. $L_{s4}$ and $L_{s5}$ ( $Ra = 9976$ )

Figure 14 shows the time evolution of the dominant horizontal mode number in the interior for the cases  $L_s = L_{s4}$  and  $L_s = L_{s5}$ . For  $L_s = L_{s4} = 0.224$ , the steady state belongs to the family of stably stratified core solutions, but the inter-plume spacing is still less than that of the final state. From figure 14(a), it can be ascertained that the evolution for the case  $L_{s4}$  is similar to that for the case  $L_{s3}$ . In figure 14(b),  $L_{s5} = 0.316$  is very close to  $L_m$  so that the base state evolves directly to the final state, with the dominant interior horizontal wavenumber fluctuating within a small range.

### 5.4. $L_{s6}$ ( $Ra = 9976$ )

Figure 15 shows the evolution for the case  $L_s = L_{s6} = 0.501$ , which is much larger than  $L_m$ . As demonstrated using secondary stability analysis, this wide-aspect-ratio convective state is strongly unstable to a wall mode. At early times, a series of proto-plumes generated from the upper and lower boundary layers continually feed the background mega-plumes (figure 15b,c), creating a quasi-periodic flow state. Moreover, for a short time, the dominant interior horizontal wavenumber for this unsteady flow remains constant at  $L_{s6}$ , hence the inter-plume spacing remains much larger than  $L_m$ . However, due to the strong boundary instability some proto-plumes grow and split the wider mega-plumes into narrower ones. This process continues

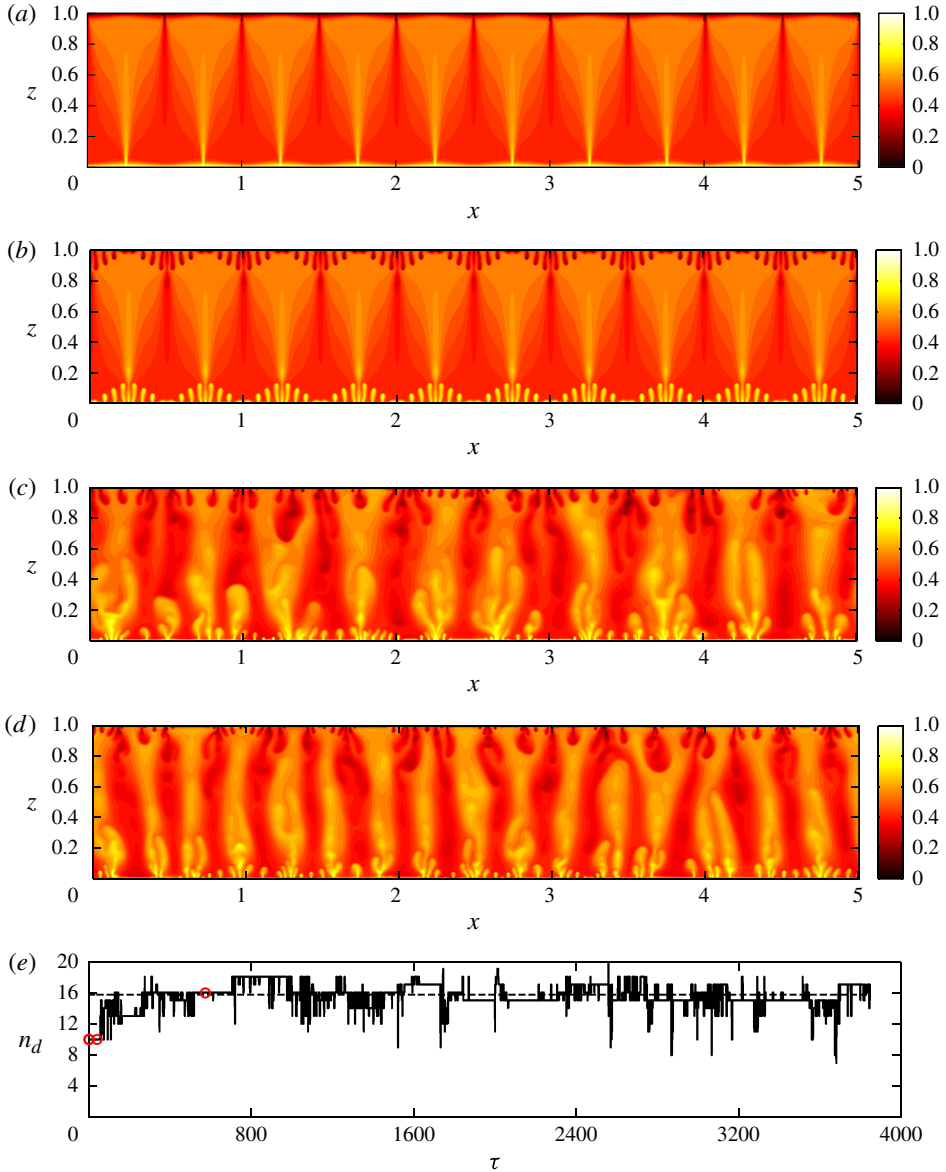


FIGURE 15. (Colour online) Snapshots of the temperature field from DNS showing the nonlinear evolution of the fastest-growing secondary instability mode for  $L_{s6} = 0.5012$ ,  $L = 10L_{s6}$ ,  $Ra = 9976$ : (a)  $\tau = 0$ ; (b)  $\tau = 1.50$ ; (c)  $\tau = 40.40$ ; (d)  $\tau = 573.64$ . (e) The time evolution of the dominant horizontal mode number  $n_d$  at  $z = 0.5$  (solid line). The dashed line shows the time-average dominant mode number and the circles correspond to the times highlighted in (a–d).

until the flow converges to the final state. Thus, there is only a single stage of evolution for this case: the strong boundary instability dominates the evolution of both the initial steady state and the ensuing unsteady flow with large  $L_s$ , generating boundary plumes that ultimately split the wide-aspect-ratio interior mega-plumes. This boundary instability becomes much stronger as  $L_s$  increases.



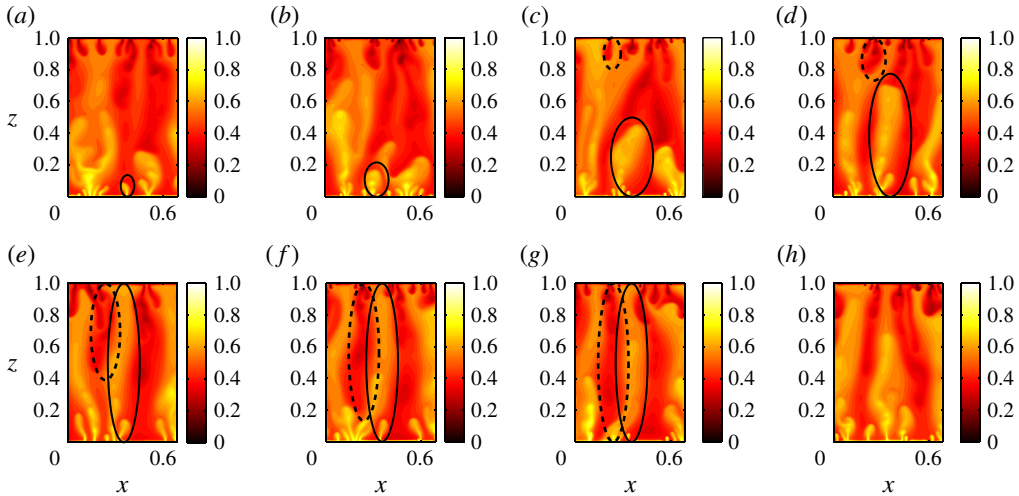


FIGURE 16. (Colour online) The splitting process from a wider plume to a narrower one,  $L_{s6} = 0.5012$ ,  $L = 10L_{s6}$ ,  $Ra = 9976$ : (a)  $\tau = 40.4$ ; (b)  $\tau = 43.4$ ; (c)  $\tau = 47.9$ ; (d)  $\tau = 51.4$ ; (e)  $\tau = 56.4$ ; (f)  $\tau = 59.9$ ; (g)  $\tau = 61.9$ ; (h)  $\tau = 68.8$ . The solid ellipse marks the growing process for the hot plume and the dashed ellipse marks the growing process for the cold plume. Only the portion of the domain  $0 \leq x \leq 0.69$  is shown to highlight the plume splitting process.

As noted above, only a fraction of the growing proto-plumes successfully split the wide mega-plumes. Figure 16 shows this plume splitting process. Initially, a small (warm) proto-plume is generated near the lower wall because of the boundary-localised instability (figure 16a). Shortly thereafter, many smaller proto-plumes generated around its root merge with the primary proto-plume, accelerating its growth (figure 16b,c). Meanwhile, another (cold) proto-plume is generated near the upper wall and grows downward (figure 16c,d). The upward growing plume soon reaches the upper wall, forming a mega-plume (figure 16e). Near the bottom wall, this mega-plume begins to merge with its neighbouring warm mega-plume; however, the growing cold plume disrupts this merging process by splitting the wider root into two narrower roots (figure 16f). Finally, the cold plume reaches the bottom wall, forming another downwelling mega-plume (figure 16g). Hence, the wider plume is successfully split into two narrower ones (figure 16h).

### 5.5. $L_{s1}$ ( $Ra = 50\,000$ )

As described in § 2, the conduction solution is linearly stable in domains of sufficiently small aspect ratio ( $L < L_c$ ). This solution is, of course, linearly unstable at larger  $L$ . We note that since the wavenumber of the fastest-growing mode  $k_f = \pm(\pi\sqrt{Ra} - \pi^2)^{1/2}$ , the corresponding wavelength  $2\pi/k_f$  is larger than the mean inter-plume spacing measured from DNS at large  $Ra$ , e.g. at  $Ra = 50\,000$ . To illustrate the nonlinear evolution of a non-convective base flow with very small  $L_s = L_{s1} \leq L_c$  in the high- $Ra$  regime, the conduction solution plus its most unstable perturbation at  $Ra = 50\,000$  is used as the initial condition for DNS in a larger domain with  $L = 10L_f$ . From figure 17, we see that at early times the flow evolves in accord with the predictions of linear theory (see (2.9) and figure 17b,c). However, after a short while, thermal

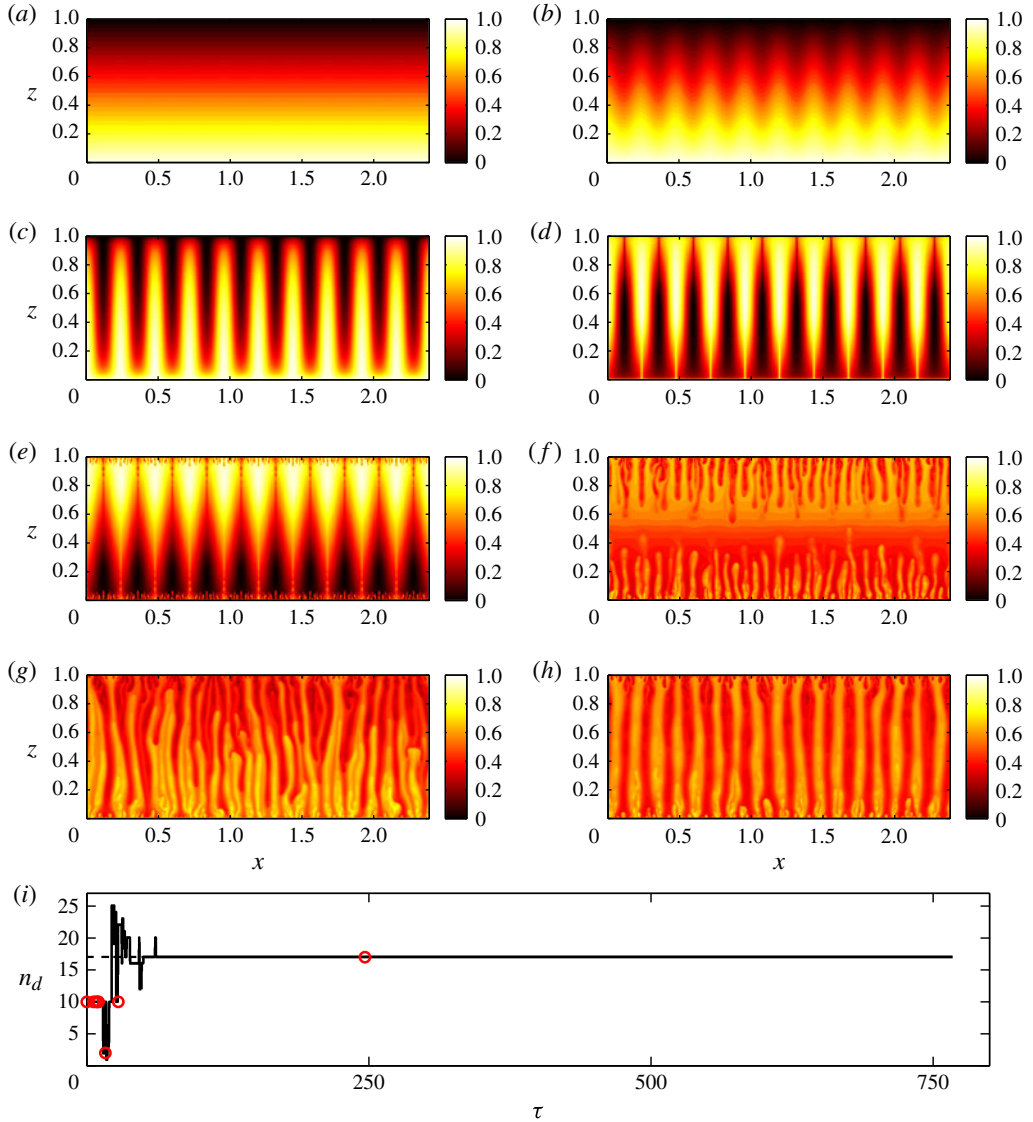


FIGURE 17. (Colour online) Snapshots of the temperature field from DNS showing the nonlinear evolution of the fastest-growing linear instability mode for any  $L_{s1} \leq L_c$ ,  $L = 10L_f$  ( $L_f = 0.2387$ ),  $Ra = 50\,000$ : (a)  $\tau = 0$ ; (b)  $\tau = 6$ ; (c)  $\tau = 8.25$ ; (d)  $\tau = 9.5$ ; (e)  $\tau = 10.5$ ; (f)  $\tau = 16.5$ ; (g)  $\tau = 28$ ; (h)  $\tau = 227$ . (i) The time evolution of the dominant horizontal mode number  $n_d$  at  $z = 0.5$  (solid line). The circles correspond to the times highlighted in (a–h).

boundary layers form near the upper and lower walls, and in the interior the flow develops a stably stratified structure (with hot/lighter fluid above cold/heavier fluid, figure 17d). This structure is similar to that of the steady stably stratified core solution at large  $L_s$ . Since the inter-plume spacing is comparably large, a boundary instability dominates the subsequent evolution, with many small proto-plumes generated near the walls (figure 17e). Unlike the previous cases in which the proto-plumes merge into the

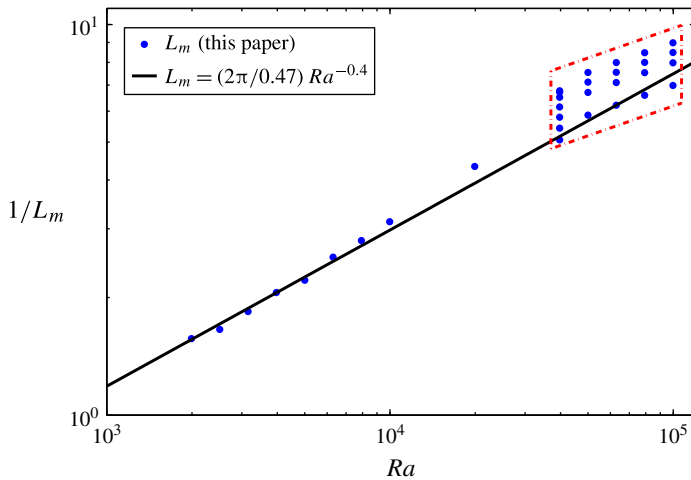


FIGURE 18. (Colour online) Variation of mean inter-plume spacing with  $Ra$ . The points have been computed from the DNS reported here; the solid line marks the fitted mean inter-plume spacing measured from the DNS of Hewitt *et al.* (2012). The DNS performed in this study were carried out in a domain with aspect ratio  $L = 10L_f$  for  $39\,716 \leq Ra \leq 99\,763$ ; a domain with  $L = 11L_f$  was also used for  $Ra = 39\,716$ . For  $Ra \leq 19\,905$ , the dominant interior horizontal mode varies (in time) within a small range so that  $L_m$  can be determined by taking a long-time average of the inter-plume spacing. However, for  $Ra \geq 39\,716$ , the interior flow becomes very well organised and (apparently) can be statistically steady for a band of wavenumbers (the dash-dotted box).

background mega-plumes, the strong stable stratification in the core prevents the warm and cold plumes from penetrating across the domain. Instead, these proto-plumes impact near the mid-plane (figure 17*f*). After a series of plume merging and splitting events, the flow evolves to the final state (figure 17*g,h*). Figure 17(*i*) shows the evolution of the dominant interior mode number for this scenario.

### 5.6. Statistical inter-plume spacing up to $Ra = O(10^5)$

From the preceding discussion, we conclude that for large  $Ra$  the final mean inter-plume spacing is determined by a balance between (suitably generalised) bulk-mode and wall-mode instabilities. When the inter-plume spacing is small, the bulk mode controls the instability, causing plume merger and coarsening of the convective pattern; when the inter-plume spacing is large, the wall-mode instability dominates, causing small plumes generated from the walls to split the wider plumes into narrower ones. To find the mean inter-plume spacing at which the effects of these two instabilities balance, we performed DNS up to  $Ra = O(10^5)$  and measured  $L_m$  by taking a long-time average of the inter-plume spacing. Our results are plotted in figure 18. Interestingly, for  $Ra \geq 39\,716$ , the interior flow becomes very well organised and appears to be metastable within a band of wavenumbers. For instance, at  $Ra = 50\,000$ , given different initial conditions, there can exist 14, 16, 17 or 18 plumes in a domain with  $L = 10L_f$ . These numerical experiments suggest that very long averaging times and very wide domains are required to firmly establish the nonlinear scale selection manifested in turbulent porous medium convection. In particular, our data arguably could be fitted by scaling relations of the form  $L_m \sim Ra^\alpha$  with  $\alpha \neq -0.4$ , the exponent proposed by Hewitt *et al.* (2012).

## 6. Conclusion

We have examined the form, stability and nonlinear evolution of initially steady cellular porous medium convection in the high- $Ra$  regime as a function of the domain aspect ratio. Our results show that the steady solutions capture certain features characterising the turbulent columnar flows observed in DNS. For steady states with small aspect ratio  $L_s$  (but for which  $L_s > L_c$ , the linear stability boundary), the steady flow has a heat-exchanger structure in the interior: the vertical advection of the horizontal-mean temperature is precisely balanced by the lateral diffusion of the fluctuation temperature field associated with a single horizontal Fourier mode. However, as  $L_s$  increases, the interior flow develops a stably stratified core involving many Fourier modes; moreover, the interior fluctuation fields are not depth-independent, also unlike their heat-exchanger counterparts. By comparing these equilibrium solutions with the time-averaged columnar flow in DNS, we find that the interior part of the mean columnar convection is neither a heat exchanger nor a stably stratified core flow, but rather blends certain features of these two steady solutions. Our results indicate that  $L_h$ , the maximum  $L_s$  at which the strictly steady heat-exchanger solution exists, is almost half of the mean inter-plume spacing  $L_m$  measured from the DNS. Furthermore, heat transport in steady porous medium convection is confirmed to be less efficient than that occurring in turbulent convection. Specifically, steady convection has a ridge of maximum  $Nu$  in  $(Ra, L_s)$  parameter space along the curve  $L_s \sim Ra^{-0.52}$ , with  $Nu \sim Ra^{0.6}$  along this ridge.

Linear stability analysis of these fully nonlinear steady states indicates that the steady solutions are most unstable at large  $Ra$  to one of two types of secondary modes. For small  $L_s$ , the most unstable disturbance is a bulk mode having roughly three to five times the wavelength of the steady convective state. The bulk instability intensifies as  $L_s$  is reduced. For large  $L_s$ , the most unstable disturbance has a growth rate that is essentially independent of horizontal scale and a vertical structure that is strongly localised near the walls. The growth rate of this wall mode increases as  $L_s$  increases and is generally an order of magnitude larger than that of the bulk mode. The nonlinear evolution of unstable steady convective states suggests that these two types of secondary instability play a primary role in determining the mean inter-plume spacing realised in turbulent porous medium convection. When the inter-plume spacing is small, the bulk mode drives the instability, causing plume merging and coarsening of the convective pattern; when the inter-plume spacing is large, the wall-mode instability dominates, causing small plumes generated from the walls to split the wider plumes into narrower ones. For generic initial conditions, this to-and-fro process continues until there is a balance between the effects of these two types of instability. We note that for the particular case in which a conduction solution is established at large  $Ra$  and then subjected to a broad spectrum of small-amplitude disturbances, the fastest-growing linear mode will dominate the early evolution. As shown in § 5.5, the flow evolves towards a steady convective state that necessarily has a lateral scale  $\approx L_f$  (the wavelength of the fastest-growing linear mode) that is larger than the final mean inter-plume spacing. In this scenario, too, the dominant secondary instability by which the resulting quasi-steady flow initially approaches the final mean inter-plume spacing  $L_m$  observed in statistically steady turbulent porous medium convection is the wall mode rather than the bulk mode identified in Hewitt *et al.* (2013).

Our DNS show that, in sufficiently wide domains, for  $Ra \leq 19976$  the dominant wavelength of the interior columnar flow may vary with time within a small range (figure 15e). In contrast, for  $Ra \geq 39716$ , the dominant interior wavelength remains

constant at sufficiently large times (figure 17*i*). Interestingly, our simulations suggest that this final inter-plume spacing is not unique but may itself fall within some small band. Although more simulations are required to determine the boundaries of this band, it is clear that the precise high-*Ra* scaling of the mean interior inter-plume spacing in statistically steady porous medium convection remains to be firmly established and will require extremely long simulations in very wide computational domains.

### Acknowledgements

We thank C. Doering, D. Hewitt and K. Shao for helpful discussions. This work was supported in part by NSF Award DMS-0928098 (G.P.C.). All of the authors are grateful for the hospitality of the Geophysical Fluid Dynamics Program at Woods Hole Oceanographic Institution, supported by NSF and ONR, where some of this work was completed.

### REFERENCES

- AIDUN, C. K. & STEEN, P. H. 1987 Transition to oscillatory convective heat transfer in a fluid-saturated porous medium. *J. Thermophys. Heat Transfer* **1**, 268–273.
- BEJAN, A. 2013 *Convection Heat Transfer*, 4th edn. Wiley.
- BOYD, J. P. 2000 *Chebyshev and Fourier Spectral Methods*, 2nd edn. Dover.
- BUSSE, F. H. 1967 The stability of finite amplitude cellular convection and its relation to an extremum principle. *J. Fluid Mech.* **30**, 625–649.
- BUSSE, F. H. 1972 The oscillatory instability of convection rolls in a low Prandtl number fluid. *J. Fluid Mech.* **52**, 97–112.
- CHINI, G. P., JULIEN, K. & KNOBLOCH, E. 2009 An asymptotically reduced model of turbulent Langmuir circulation. *Geophys. Astrophys. Fluid Dyn.* **103**, 179–197.
- CLEVER, R. M. & BUSSE, F. H. 1974 The oscillatory instability of convection rolls in a low Prandtl number fluid. *J. Fluid Mech.* **65**, 625–645.
- CORSON, L. T. 2011 Maximizing the heat flux in steady unicellular porous media convection. In *Geophysical Fluid Dynamics Program Report*, Woods Hole Oceanographic Institution.
- ELDER, J. W. 1967 Steady free convection in a porous medium heated from below. *J. Fluid Mech.* **27**, 29–48.
- FOWLER, A. C. 1997 *Mathematical Models in the Applied Sciences*. Cambridge University Press.
- GRAHAM, M. D. & STEEN, P. H. 1992 Strongly interacting traveling waves and quasiperiodic dynamics in porous medium convection. *Physica D* **54**, 331–350.
- GRAHAM, M. D. & STEEN, P. H. 1994 Plume formation and resonant bifurcations in porous-media convection. *J. Fluid Mech.* **272**, 67–90.
- HERBERT, T. 1983 Secondary instability of plane channel flow to subharmonic three-dimensional disturbances. *Phys. Fluids* **26**, 871–874.
- HERBERT, T. 1988 Secondary instability of boundary layers. *Annu. Rev. Fluid Mech.* **20**, 487–526.
- HEWITT, D. R., NEUFELD, J. A. & LISTER, J. R. 2012 Ultimate regime of high Rayleigh number convection in a porous medium. *Phys. Rev. Lett.* **108**, 224503.
- HEWITT, D. R., NEUFELD, J. A. & LISTER, J. R. 2013 Stability of columnar convection in a porous medium. *J. Fluid Mech.* **737**, 205–231.
- HEWITT, D. R., NEUFELD, J. A. & LISTER, J. R. 2014 High Rayleigh number convection in a three-dimensional porous medium. *J. Fluid Mech.* **748**, 879–895.
- HORNE, R. N. & O'SULLIVAN, M. J. 1974 Oscillatory convection in a porous medium heated from below. *J. Fluid Mech.* **66**, 339–352.
- HORTON, C. W. & ROGERS, F. T. 1945 Convection currents in a porous medium. *J. Appl. Phys.* **16**, 367–370.

- KELLY, R. E. 1967 On the stability of an inviscid shear layer which is periodic in space and time. *J. Fluid Mech.* **27**, 657–689.
- KIMURA, S., SCHUBERT, G. & STRAUS, J. M. 1986 Route to chaos in porous-medium thermal convection. *J. Fluid Mech.* **166**, 305–324.
- KIMURA, S., SCHUBERT, G. & STRAUS, J. M. 1987 Instabilities of steady, periodic, and quasi-periodic modes of convection in porous media. *Trans. ASME J. Heat Transfer* **109**, 350–355.
- LAPWOOD, E. R. 1948 Convection of a fluid in a porous medium. *Proc. Camb. Phil. Soc.* **44**, 508–521.
- METZ, B., DAVIDSON, O., DE CONINCK, H., LOOS, M. & MEYER, L. 2005 *IPCC Special Report on Carbon Dioxide Capture and Storage*. Cambridge University Press.
- NIELD, D. A. & BEJAN, A. 2006 *Convection in Porous Media*, 3rd edn. Springer.
- ORSZAG, S. A. & PATERA, A. T. 1983 Secondary instability of wall-bounded shear flows. *J. Fluid Mech.* **128**, 347–385.
- OTERO, J., DONTCHEVA, L. A., JOHNSTON, H., WORTHING, R. A., KURGANOV, A., PETROVA, G. & DOERING, C. R. 2004 High-Rayleigh-number convection in a fluid-saturated porous layer. *J. Fluid Mech.* **500**, 263–281.
- PALM, E., WEBER, J. E. & KVERNVOLD, O. 1972 On steady convection in a porous medium. *J. Fluid Mech.* **54**, 153–161.
- PHILLIPS, O. M. 1991 *Flow and Reactions in Permeable Rocks*. Cambridge University Press.
- PHILLIPS, O. M. 2009 *Geological Fluid Dynamics: Sub-surface Flow and Reactions*. Cambridge University Press.
- SCHUBERT, G. & STRAUS, J. M. 1982 Transitions in time-dependent thermal convection in fluid-saturated porous media. *J. Fluid Mech.* **121**, 301–313.
- TANDON, A. & LEIBOVICH, S. 1995 Secondary instabilities in Langmuir circulations. *J. Phys. Oceanogr.* **25**, 1206–1217.
- WEN, B., CHINI, G. P., DIANATI, N. & DOERING, C. R. 2013 Computational approaches to aspect-ratio-dependent upper bounds and heat flux in porous medium convection. *Phys. Lett. A* **377**, 2931–2938.